1   **Impacts of ice-nucleating particles from marine aerosols on mixed-phase orographic clouds**

2   **during 2015 ACAPEX field campaign**

4   Yun Lin[1,2], Jiwen Fan[1,*], Pengfei Li[3,4], L. Ruby Leung[1], Paul J. DeMott[5], Lexie Goldberger[1],

5   Jennifer Comstock[1], Ying Liu[1], Jong-Hoon Jeong[1,2], Jason Tomlinson[1]

7   [1] Atmospheric Sciences and Global Change Division, Pacific Northwest National Laboratory,

8   Richland, WA 99352

9   [2] Joint Institute for Regional Earth System Science and Engineering (JIFRESSE), University of

10   California, Los Angeles (UCLA), Los Angeles, CA 90064

11   [3] College of Science and Technology, Hebei Agricultural University, Baoding, Hebei

12   14 071000, P.R. China

13   [4] Research Center for Air Pollution and Health; Key Laboratory of Environmental

14   Remediation and Ecological Health, Ministry of Education, College of Environment and

15   Resource Sciences, Zhejiang University, Hangzhou, Zhejiang 310058, P.R. China

16   [5] Department of Atmospheric Science, Colorado State University, Fort Collins, CO 80523, USA

18   Corresponding author: Jiwen Fan (jiwen.fan@pnnl.gov)

Abstract

A large fraction of annual precipitation over the western United States comes from wintertime orographic clouds associated with atmospheric rivers (ARs). Transported African and Asian dust and marine aerosols from the Pacific Ocean may act as ice-nucleating particles (INPs) to affect cloud and precipitation properties over the region. Here we explored the effects of INPs from marine aerosols on orographic mixed-phase clouds and precipitation at different AR stages for an AR event observed during the 2015 ACAPEX field campaign under low dust (< 0.02 cm^{-3}) conditions. Simulations were conducted using the chemistry version of the Weather Research and Forecasting model coupled with the spectral-bin microphysics at 1-km grid spacing, with ice nucleation connected with dust and marine aerosols. By comparing against airborne and ground-based observations, accounting for marine INP effects improves the simulation of cloud phase state and precipitation. The marine INPs enhance the formation of ice and snow, leading to less shallow warm clouds but more mixed-phase and deep clouds, and increased ice water path (over 5 times) and snow precipitation (over 40 times). The responses of cloud and precipitation to marine INPs vary with the AR stages with more significant effects before AR landfall and post-AR than after AR landfall, mainly because the moisture and temperature conditions change with the AR evolution. This work suggests weather and climate models need to consider the impacts of marine INPs since their contribution is notable under low dust conditions despite the much lower relative ice nucleation efficiency of marine INPs.

1 Introduction

Atmospheric river (AR) events have great impacts on atmospheric and hydrological processes in the western United States during winter. On a long-term average, AR storms contribute to 20–50% of California's precipitation totals (Dettinger et al., 2011). Understanding the factors influencing different types of precipitation (rain vs. snow) associated with ARs is crucial for planning and managing regional water resources and hydrologic hazards and improving atmospheric and hydrologic forecasting in the western United States. Rain and snow precipitation produced by orographic clouds over the Sierra Nevada Mountains is closely related to the partitioning between cloud liquid and ice phases, which can be largely modified by aerosol particles (Rosenfeld et al., 2013; Fan et al., 2014, 2017b). However, aerosol-orography-precipitation relationships are complicated, depending on aerosol properties, mountain geometry, cloud phase, temperature, humidity, and flow patterns as reviewed in Chouldhury et al. (2019).

Over the western United States, understanding the roles of aerosols, particularly those capable of initiating ice crystal formation in altering clouds and precipitation is still limited, which has motivated recent observational and modeling studies (Ault et al., 2011; Creamean et al., 2013, 2015; Rosenfeld et al., 2013; Fan et al., 2014, 2017b; Martin et al., 2019; Levin et al., 2019). While it has been found that long-range transported aerosols particularly dust particles as ice nucleating particles (INPs) influence clouds and precipitation in the mountainous western United States (Uno et al., 2009; Ault et al., 2011; Creamean et al., 2013), it is also clear from measurements that clouds occurring in and around ARs can also be influenced by INPs with apparent sources from the ocean (Levin et al., 2019).

Previous studies showed that INPs can increase total precipitation through the "seeder feeder" mechanism (Choularton and Perry, 1986; Creamean et al., 2013), in which ice crystals

65   that form in the upper portions of orographic clouds can collect droplets and grow to a larger size

66   as they fall through a supercooled liquid layer before reaching the ground. Fan et al. (2014,

67   2017b) found that INPs like dust particles can increase precipitation by enhancing riming and

68   deposition processes in mixed-phase orographic clouds, consistent with other studies (e.g.,

69   Muhlbauer and Lohmann, 2009; Xiao et al., 2015; Hazra et al., 2016; Yang et al., 2020). Fan et

70   al. (2017a) also noted that the relative importance of riming to deposition depends on the mixed-

71   phase cloud temperatures. Despite the importance of INPs in cloud formation and precipitation,

72   they typically have a low abundance and large variations in their nucleating characteristics,

73   especially in terms of the temperatures over which they initiate ice crystal formation (Kanji et al.,

74   2017; Levin et al., 2019). Hence, there is large uncertainty in evaluating INPs impacts on mixed-

75   phase and ice clouds as well as precipitation.

76   Dust and biological particles are known INPs. Biological particles can cause freezing at

77   temperatures as warm as −5 °C (Murray et al., 2012). During ARs, the long-range transport of

78   dust or biological particles is highly episodic (Creamean et al., 2013). Sea spray or marine

79   aerosols consisting of sea salt and marine organic carbon resulting from wave breaking and

80   bubble bursting at the ocean surface may also be a source of INPs (Burrows et al., 2013;

81   Vergara-Temprado et al., 2017; McCluskey et al., 2018b; Levin et al., 2019). Recently,

82   McCluskey et al. (2018a) derived an ice nucleation parameterization for INPs from sea spray

83   aerosols based on observations collected at a North Atlantic coastal site and its relation to the

84   marine aerosol surface area. Given the distinct physio-chemical characteristics and the different

85   ice-nucleating efficiency (magnitudes lower than mineral dust; McCluskey et al. 2018a), the

86   impact of marine INPs on cloud and precipitation could be very different from dust or biological

87   particles (DeMott et al., 2016; Kanji et al., 2017). However, studies of marine-sourced INP

88   effects on clouds and associated precipitation are limited (Kanji et al., 2017; Levin et al., 2019).

89   A few previous studies investigated the impacts of marine INPs on precipitation and radiation

90   with global climate models (Hoose et al., 2010; Burrows et al., 2013; Yun and Penner, 2013),

91   albeit without the advantage of direct data on their ice nucleation efficiencies. Further, a detailed,

92   process-level understanding of how marine INPs affect mixed-phase cloud processes and

93   precipitation is lacking.

94   Following the CalWater campaigns in 2009, 2011, 2014, an interagency sponsored study,

95   CalWater 2015, utilized a larger suite of instruments and measurement platforms to study ARs

96   and aerosol-cloud interactions in AR environments (Ralph et al., 2016). As part of CalWater

97   2015, the U.S. Department of Energy sponsored Atmospheric Radiation Measurement (ARM)

98   Cloud Aerosol Precipitation Experiment (ACAPEX) field campaign aimed specifically at

99   improving understanding and modeling of aerosol impacts on winter storms associated with

100   landfalling ARs (Leung et al., 2016). The ACAPEX campaign conducted intensive sampling of

101   clouds and aerosols using instruments on board the ARM Aerial Facility Gulfstream (G-1)

102   aircraft and ARM Mobile Facility on board the research vessel Ron Brown. These measurements

103   were made in conjunction with clouds and aerosols, meteorological, hydrological, and oceanic

104   measurements collected by instruments on three other aircraft and Ron Brown and at a coastal

105   surface station. Collectively, these data provide a unique opportunity to examine the complex

106   interactions among aerosols, orographic clouds, and ARs.

107   A major AR event spanning over 5 - 9 February 2015 occurred during the ACAPEX

108   campaign, producing heavy rainfall with some regions receiving up to 400 mm of total

109   precipitation during the event (Ralph et al., 2016; Cordeira et al., 2017). This AR event was

110   extensively sampled by the G-1 aircraft (Schmid et al., 2014) for characterizing aerosol and

111   cloud properties. During this event, marine aerosols were the main aerosol type and marine INPs

112   were dominant at cloud activation temperatures. Aerosol sampled by G-1 indicated that dust and

113   biological particles were rather scarce in and around ARs, which is in stark contrast to the

114   dominance of dust INPs during the AR events in the CalWater 2011 campaign (Levin et al.,

115   2019). Therefore, the AR event during the ACAPEX campaign provides a rather unique

116   opportunity to explore the role of marine aerosols in the orographic clouds and precipitation

117   associated with landfalling ARs in the western United States.

118   In our previous modeling studies (Fan et al., 2014, 2017b), we implemented an

119   immersion freezing parameterization for dust particles (DeMott et al. 2015) in a spectral-bin

120   microphysics (SBM) scheme to examine the long-range dust effects on AR-associated

121   orographic mixed-phase clouds and precipitation during CalWater 2011. With marine INPs

122   dominating in CalWater 2015/ACAPEX, in this study we implemented the recently developed

123   ice immersion nucleation parameterization for sea spray aerosols by McCluskey et al. (2018b) in

124   the SBM scheme. To explicitly simulate various aerosol types, different from Fan et al. (2014,

125   2017a) who prescribed aerosols based on observations, a chemistry version of the Weather

126   Research and Forecasting model (WRF-Chem) coupled with the SBM (Gao et al., 2016) was

127   employed to predict aerosol properties and their interactions with clouds and radiation for the AR

128   event on 6 - 9 February 2015. We focused on exploring the effects of INPs from sea spray

129   aerosols, in competition with mineral dust INPs, on the orographic mixed-phase clouds and

130   precipitation at different stages of the AR event as thermodynamic conditions evolved with the

131   different AR stages.

2 Model configuration and experiment design

The WRF-Chem version 3.6 coupled with SBM as described in Gao et al. (2016) is employed for model simulations of this study, in which SBM is coupled with the Model for Simulating Aerosol Interactions and Chemistry (MOSAIC; Fast et al., 2006; Zaveri et al., 2008). The SBM scheme is a fast version in which ice crystal and snow (aggregates) are represented with a single size distribution (low-density ice) with a separation at 150 μm in radius, and graupel or hail is for high-density ice represented with an additional size distribution (Khain et al., 2009, 2010; Fan et al., 2012, 2017a). Here we choose the graupel version since hail is not one of the major cloud hydrometeors in the case we simulate. The fall speed power law relationships for ice/snow and graupel are depicted in Xue et al. (2017). The WRF-Chem-SBM model is particularly designed to improve simulations of aerosol effects on clouds for complicated aerosol compositions and heterogeneous spatial distribution of aerosols. It has been applied in several studies including warm stratocumulus clouds (Gao et al., 2016), thunderstorms (Fan et al. 2020; Zhang et al., 2020), and supercell storms (Lin et al., 2020). Here WRF-Chem-SBM is employed, different from our previous studies in Fan et al. (2014, 2017a) which used WRF-SBM with prescribed aerosols, in order to explicitly simulate various aerosol types including marine aerosols and dust particles.

The four-sector MOSAIC aerosol module is chosen for the simulations of aerosols and the CBMZ (Carbon Bond Mechanism version Z) is used for gas-phase chemistry. The MOSAIC module treats nine major aerosol species (sulfate, nitrate, chloride, ammonium, sodium, black carbon, primary organics, other inorganics (OIN), and water). OIN is used as a surrogate of dust and the production of dust is parameterized with the dust transport model DUSTRAN (Shaw et al., 2008). Sea salt aerosol (a combination of sodium and chloride), as a surrogate for all SSA, is

155 parameterized as a function of sea-surface wind speed (Gong et al., 1997b, a). The dry diameters

156 of the particles over the four bins have a range of 0.039–0.156, 0.156–0.624, 0.624–2.5, and 2.5–

157 10.0 μm, respectively. For the total aerosol, aerosol size distribution over each section is

158 represented with a 2-moment approach that predicts aerosol mass and number following a log-

159 normal distribution (Simmel and Wurzler, 2006). For each composition such as dust and sea salt,

160 only the mass mixing ratio in each section is predicted and outputted. The aerosol number

161 mixing ratio in each bin is only predicted for the total aerosol. Therefore, in this study, the dust

162 and sea salt number mixing ratios used for ice nucleation parameterizations were derived based

163 on their respective mass mixing ratios by assuming the same size and density of all particles over

164 each bin, that is,

165
$$N_{i,j} = \frac{m_j}{6\pi (D_j)^3 \rho_i}$$

166 where i denotes the aerosol composition (sea salt or dust here), j denotes the jth aerosol bin, m_j is

167 the total mass mixing ratio of the jth bin, ρ_i is the assumed density (i.e., 2.6 g cm^{-3} for dust and

168 2.2 g cm^{-3} for sea salt), and D_j is the geometric mean diameter of jth bin. The approach for

169 deriving the number mixing ratio for each aerosol component has been used in the literature (i.e.,

170 Zhao et al., 2013). We understand that the assumption that all particles have the same size over

171 each bin may introduce some uncertainty. However, the size distribution of each aerosol

172 component is unknown in the model and any assumption on the size distribution might introduce

173 uncertainty.

174
175 **2.1 Implementing immersion freezing parameterization for marine INPs**

176 In the original SBM model, the ice nucleation accounting for both deposition ice

177 nucleation and condensation-freezing is parameterized based on Meyers et al. (1992) and Bigg

178   (1953) is employed for immersion and homogeneous drop freezing. Neither of the ice nucleation

179   parameterizations is connected with aerosols. Bigg (1953) was formulated based on the

180   stochastic hypothesis where the freezing probability is assumed proportional to drop mass and

181   the freezing rate is as a function of temperature without involving INPs. Fan et al. (2014, 2017a)

182   implemented DeMott et al. (2015) as an immersion freezing parameterization to investigate the

183   effects of dust INPs on orographic mixed-phase clouds and precipitation during CalWater 2011.

184   We adapted this implementation to WRF-Chem-SBM for this study to connect ice nucleation

185   with dust particles. Developed based on both laboratory data and field measurements, DeMott et

186   al. (2015) is an empirical parameterization for immersion freezing of natural mineral dust

187   particles. INP concentrations are quantified as functions of temperature and the total number

188   concentration of particles larger than 0.5 μm diameter. In our implementation, the dust number

189   mixing ratio for each aerosol bin is derived from its mass as detailed in the section above. The

190   total dust number mixing ratio inputted to DeMott et al. (2015) is the integration over 0.5 -10

191   μm.

192   To connect ice nucleation with sea spray aerosols, we implemented McCluskey et al.

193   (2018a, thereafter MC2018), which was developed for quantifying ice nucleating activity by

194   marine organics over the North Atlantic Ocean, in SBM following a similar approach as the

195   implementation of DeMott et al. (2015). The nucleation site density in MC2018 is described as

196   $$n_s = exp(-0.545(T - 273.15) + 1.012)$$

197   where n_s is the nucleation site density (m^{-2}) and T is the temperature (K). With n_s determined by

198   MC2018, the nucleated ice particle concentration is obtained following Niemand et al. (2012) as

199   $$\sum_{j=1}^{n} N_j = \sum_{j=1}^{n} N_{tot,j}\{1 - exp[-S_{ae,j}n_s(T)]\}$$

200 where $S_{ae,j}$ is the surface area of individual sea spray aerosol particles in the jth bin which is

201 calculated from $\pi D_j^2/4$ (D_j is the geometric-mean diameter), $N_{tot,j}$ is the total sea spray aerosol

202 number in each bin which is derived from its mass as detailed in the section above, and N_j is the

203 ice particle number in each bin. Sea salt particles are used as the surrogate of sea spray aerosols

204 given that most marine organic aerosols exist with coating on the surface of sea salt particles in

205 the size range that dominates surface area (e.g., Prather et al., 2013).

206   Bigg et al. (1953) is employed only for homogeneous drop freezing when the temperature

207 is colder than -37 °C. As discussed in Fan et al. (2014), the deposition-condensation freezing is

208 turned off because the simulation with deposition-condensation freezing produces a large

209 number of small ice particles, which is not consistent with the observed mixed-phase cloud

210 properties in the study region. Contact freezing is also turned off due to negligible contributions

211 (Fan et al., 2014).

212 **2.2 Experiment design**

213   Simulations are configured with two nested domains using the nesting down approach

214 (i.e., the inner domain is run separately driven by the outer domain), covering most of the

215 western US (Fig. 1). The outer domain consists of 399 × 399 grid points with a horizontal grid

216 spacing of 3 km and the inner domain consists of 498 × 390 grid points with a horizontal grid

217 spacing of 1 km. 50 vertical levels with stretched intervals are configured, with a grid spacing of

218 70 m at the lowest levels and ~400 m at the model top. The dynamics time step is 15 seconds for

219 the outer domain and 5 seconds for the inner domain.

220   The simulation for the outer domain starts at 00:00 UTC on February 3 and runs for 48

221 hours for chemistry spin-up using the WRF-Chem-SBM model, driven by global WRF-Chem

222 simulation as the initial and boundary conditions of gas-phase species and aerosols and the

223 Modern-Era Retrospective analysis for Research and Applications, Version 2 (MERRA2; spatial

224 resolution of 0.5 by 0.5 degree and temporal resolution of 6-hourly) as the initial and boundary

225 conditions of meteorological fields. Then the outer domain simulation is reinitialized at 00:00 UTC

226 on February 5 using the meteorological data from MERRA2 to avoid the large error growth in

227 meteorology associated with long-time model integration, although the chemistry simulation is a

228 continuation from the spin-up run and runs until 23:00 UTC on February 8. Given that running the

229 WRF-Chem-SBM fully-coupled model is extremely computationally expensive for 1-km grid

230 spacing in the inner domain, we interpolate aerosol-related quantities such as aerosol composition,

231 hygroscopicity, and mass and number concentrations from the outer domain simulations using

232 bilinear interpolation for the inner-domain simulation to reduce computational cost. This means

233 that we conduct the inner-domain simulation separately with chemistry turned off, and aerosol

234 information is updated hourly using data from the outer domain simulations. The inner-domain

235 simulation is run from 00:00 UTC on February 5 to 23:00 UTC on February 8, and the initial and

236 boundary meteorological conditions are from MERRA2. To validate this approach, we compared

237 the simulation with fully coupled WRF-Chem-SBM for the inner domain simulation and found

238 that the two simulations resemble each other in terms of precipitation (Fig. S1). Therefore, it is a

239 valid approach that saves computation time by about 40%.

240   For emissions data, the U. S. Environment Protection Agency (EPA) National Emission

241 Inventory (NEI) with a 4 km by 4 km horizontal resolution based on the year 2011 rates

242 (NEI2011) is commonly used for anthropogenic emissions in the United States. However, using

243 NEI2011 predicts too large anthropogenic aerosol mass compared with observations. Since the

244 emissions of gaseous species and particulate matter decreased significantly from 2011 to 2015 in

245 California (Table S1), the California Air Resources Board emission inventory in 2015

246 (CARB2015) is used for anthropogenic emissions input for California, while NEI2011 is used

247 for other states in the simulation domain. The use of NEI2011 for other states is acceptable since

248 the lower and middle atmosphere in the simulation domain is dominated by southwesterly winds

249 during the simulation period that transport air pollutants from coastal to inland regions. The use

250 of CARB2015 reduces the simulation of aerosol number concentrations mainly below 2 km. The

251 aerosol concentration averaged over 1-2 km altitudes is about 160 cm^{-3} with CARB2015 and 317

252 cm^{-3} with NEI2015, which is 26% lower and 47% higher than aircraft observations (215 cm^{-3}),

253 respectively. Thus, the simulated aerosol concentrations with CARB2015 are in better agreement

254 with observations.

255   The Model of Emissions of Gases and Aerosols from Nature (MEGAN) with a monthly

256 temporal and 1 km horizontal resolution (Guenther et al., 2012) is used for biogenic emissions.

257 The Rapid Radiative Transfer Model for application to GCMs (RRTMG) is used for shortwave

258 and longwave radiation schemes (Iacono et al., 2008), the Noah Land Surface Model for land

259 surface physics (Chen and Dudhia, 2001), and the Mellor-Yamada-Janjic (MYJ) scheme for

260 planetary boundary layer parameterization (Mellor and Yamada, 1982; Janjić and Prediction,

261 2001). Cumulus parameterization is not considered for the simulations over both domains.

262   Three simulations were carried out over the inner domain for this study to investigate the

263 impacts of marine INPs: (1) The reference case is Bigg, using the default immersion freezing

264 parameterization of Bigg et al. (1953) in SBM which is temperature-dependent only; (2)

265 DM15+MC18, in which both DeMott et al. (2015) and MC2018 parameterizations are used for

266 ice nucleation from dust and marine aerosols, respectively; (3) DM15, using the parameterization

267 of DeMott et al. (2015) for dust aerosols (diameter > 0.5 μm) with MC2018 turned off. The

268 impacts of marine INPs are derived by comparing the DM15+MC18 and DM15 simulations.

3 Case description and measurements

As introduced earlier, our study case is the AR event occurring during 5 - 9 February 2015 during the ACAPEX campaign and made landfall on the coast of Northern California, producing heavy rainfall. Marine aerosols were the main aerosol type. Dust and biological particles were rather scarce in and around the AR (Levin et al., 2019).

The AR evolution has three distinct stages: before AR landfall (from 06:00 UTC 5 to 18:00 UTC 6 February), after AR landfall (from 18:00 UTC 6 to 12:00 UTC 7 February), and post-AR (from 12:00 UTC 7 to 09:00 UTC 8 February). The three stages can be identified from the change of the integrated water vapor (IWV) with time during the event (Fig. 2a). Before AR landfall, IWV in most of California was relatively low (Fig. 2a, left). The IWV in northern California increased as the AR made landfall at about 18:00 UTC on 6 February and brought ample water vapor to California (Fig. 2a, middle). Heavy orographic precipitation along the Sierra Nevada Mountains occurred during this period. At 12:00 UTC 7 February, the AR started to retreat (Fig. 2a, right), and postfrontal cloud cells formed, with relatively small cloud fraction and precipitation.

Vertical profiles of the thermodynamic and kinematic environments at the three stages are shown in Figs. 2b-d. The thermodynamic and kinematic environments significantly varied with the AR stages. After AR landfall, water vapor increased significantly in the lower atmosphere (below 5 km), but the middle and upper levels became drier (dashed, Fig. 2b) compared with the stage before AR landfall (solid). The vertical motion also weakened after AR landfall (Fig. 2d), suggesting that the atmosphere became more stable. At the post-AR stage, moisture above 2-km altitude was reduced compared to after AR landfall. Note that the

292   temperature below 8 km was colder by up to 6 °C at the post-AR stage compared to the previous

293   two stages (Fig. 2c). These differences in the meteorological conditions among the different

294   stages are very important to understand the cloud and precipitation properties and their responses

295   to marine INPs.

296   Extensive in-situ and remote-sensing measurements are used to understand aerosol and

297   cloud properties and evaluate model results. The G-1 aircraft sampled the postfrontal clouds on

298   February 7 during 20:20-20:30 UTC.

299   Aerosol instruments on board the G-1 aircraft included (1) a Droplet Measurement

300   Technologies (DMT) ultrahigh sensitivity aerosol spectrometer (UHSAS), measuring dry fine

301   mode aerosol size spectra of 55–800 nm with sizing uncertainty of 2.5% (Uin, 2016); (2) a

302   Passive Cavity Aerosol Spectrometer Probe (PCASP) for coarse model aerosol spectra (0.1-3

303   μm) with +/-20% uncertainty in size and +/-16% in concentration (Goldberger, 2020), and (3)

304   Aerosol Time of Flight Mass Spectrometry (ATOFMS) measurements provided the mean

305   fractional number contributions of aerosol source classifications (Levin et al., 2019). Cloud

306   instruments include an FCDP (1.5-50 μm) with ~3 μm uncertainty in size (Glienke and Mei,

307   2020), and the two-dimensional stereo (2DS) probe with +/-10 μm size uncertainty to provide

308   cloud particle size spectra (Glienke and Mei, 2019). Uncertainty in the number concentration for

309   both probes follows Poisson's counting statistics. The LWC and IWC are derived from the Water

310   Content Monitor (WCM) on board the G-1 aircraft, an instrument that uses the impact of water

311   on several heated wires as the basis for measuring cloud total water content (TWC) and liquid

312   water content (LWC) from which the ice water content (IWC) can be derived (Baumgardner et

313   al., 2011; Matthews et al., 2015). Wind tunnel measurements indicate that ice contributes <1% to

314   the LWC elements response.

The Next Generation Radar (NEXRAD) radar reflectivity measurements were processed and used for model evaluation. The original NEXRAD Level 2 data (polar coordinate) were downloaded from AWS-NOAA NEXRAD S3 data service (https://registry.opendata.aws/noaa-nexrad/). We mapped the data to a Cartesian coordinate with 2 km horizontal resolution and approximately 5 min frequency using the Python ARM Radar Toolkit (Py-ART; Helmus and Colis, 2016). The operational NEXRAD radar reflectivity uncertainties are 2 - 3 dB (Gourley et al., 2003) and theoretical demonstrations with differing raindrop shape models yield radar reflectivity biases of 1.2 dB (Gourley et al., 2009). The observed precipitation rates are from the rain gauge measurements, provided by the NOAA Earth System Research Laboratory's Physical Sciences Division (https://psl.noaa.gov/data/obs/datadisplay).

4 Results

4.1 Model evaluation with observations

We evaluate the model simulations of aerosol and cloud properties and surface precipitation. Figure 3a shows a comparison of modeled aerosol properties including aerosol number concentration and chemical composition from the simulation of DM15+MC18 intended to represent the observed case, with the G-1 aircraft measurements on 7 February. Aerosol properties in all three simulations are similar, and thus only DM15+MC18 is shown. Overall, the simulated aerosol number concentration over the size range of 0.067 - 3 μm is comparable to the observations over the same size range estimated by combining data from UHSAS and PCASP at below 2-km altitude. The simulation overestimates the total aerosol number concentrations by ~ 2-times averaged over the altitudes of 2.2-3.2 km. At 2.8 km, the difference between the simulation (219 cm^{-3}) and observations (55 cm^{-3}) is about 4 times. The mean fractional number contributions of aerosol composition classifications measured from ATOFMS are shown in Fig.

338   3b. For comparison with the model, the mean mass contributions of the corresponding aerosol

339   source classifications are computed since the number concentrations of individual aerosol

340   components are not predicted by WRF-Chem (Fig. 3c). Both the observed fractional number

341   contributions and the simulated mass contributions show that marine aerosols are dominant

342   during the AR event, accounting for more than 60% of the total aerosol number based on

343   ATOFMS measurements and total aerosol mass based on the simulation. Although the simulated

344   dust mass fraction is ~14%, the derived number concentration for sizes larger than 0.5 μm is very

345   low (less than 0.02 cm^{-3}, shown in a later figure). This is because the dust number concentration

346   is dominated by small particles (14.71 cm^{-3} for the sizes smaller than 0.5 μm). The number

347   concentrations of the sea salt aerosols are generally three orders of magnitude higher than those

348   of dust, and these numbers populate smaller bins of the aerosol distribution (97% from the first

349   two aerosol size bins) even though the sea salt mass is predominately at larger sizes (96% from

350   the last two size bins).

351   Figure 4 presents an evaluation of precipitation, showing the accumulated precipitation

352   during the AR event from 06:00 UTC 5 February to 09:00 UTC 8 February 2015 (Fig. 4a) and

353   the time-series of mean precipitation rates averaged over the observation stations (Fig. 4b). The

354   model generally captures the spatial pattern of the observed accumulated precipitation (Fig. 4a)

355   and reproduces the temporal evolution of precipitation (Fig. 4b). Two major precipitation periods

356   in the observations, including AR-induced orographic precipitation and postfrontal precipitation,

357   are generally captured in the simulations, although the simulated postfrontal precipitation occurs

358   several hours later in the simulations compared to the observations. All three simulations predict

359   a narrower but higher peak precipitation compared with the observed wider peak with lower

360   values (Fig. 4b). However, the overestimation of the peak value by DM15+MC18 is lower than

361   the other two (30% vs. 45% for DM15 and 58% for Bigg; Fig. 4b-c). The accumulated

362   precipitation in the southern mountain range (the southern part of white boxes in Fig. 4a) is

363   generally less than 100 mm in observations and less than 120 mm in DM15+MC18 but more

364   than 140 mm in the other two simulations. The mean precipitation over the white box

365   accumulated over the AR period are 89, 128, 130, and 116 mm for observations, Bigg, DM15,

366   and DM15+MC18, respectively. Again, although all three simulations overestimate the

367   precipitation, DM15+MC18 simulates the lowest value and is closer to observations. There is a

368   clear spillover effect caused by marine INPs (white box in the right panel of Fig. 4a). That is,

369   with marine INPs, more ice/snow formed over the windward side falls slower than rain and more

370   of them are transported to the lee side. This will be discussed in more detail in section 4.2. In the

371   northern part of the domain (> 40º N), DM15+MC18 predicts more precipitation (i.e., 48 mm for

372   the mean accumulated precipitation) than the other two simulations (i.e., 45 mm in Bigg and 42

373   mm in DM15). The simulated precipitation between Bigg and DM15 is very similar (Fig. 4a),

374   suggesting that in a low dust environment, the temperature-dependent Bigg (1953)

375   parameterization simulates similar ice formation as DeMott et al. (2015).

376   Cloud phase is crucial to radiation and precipitation for mixed-phase clouds, and the

377   glaciation ratio is usually used to represent the cloud phase states. The glaciation ratio is defined

378   as IWC/(IWC+LWC), where LWC and IWC denote liquid and ice water content, respectively.

379   Values less than 0.1 and larger than 0.9 denote the liquid phase and ice phase, respectively, with

380   values between 0.1 and 0.9 for the mixed-phase (Korolev et al., 2003). The G-1 aircraft sampled

381   the postfrontal clouds on February 7 as shown in Fig. 5a. All three simulations cannot capture the

382   observed size of the precipitation cell (Figs. 5b and S2). In the simulations, precipitation is

383   dominated by a few heavy precipitation clusters instead of the observed wide precipitation area.

384 The simulated cells also do not reach the high altitudes found in the observations. The deviations

385 of the simulation from observations for the postfrontal clouds could be because of various

386 reasons such as (a) the long-time model integration time (the 4th day after model initiation) and

387 (b) the spatial mismatch of simulated and observed clouds since those postfrontal clouds are

388 small. Anyhow, DM15+MC18 simulates the largest size of the precipitation cell, with the

389 highest vertical extent among the three simulations.

390   LWC and IWC along both horizontal and vertical flight segments are displayed in Figs.

391 6a-b. IWC is generally 2-4 times larger than LWC in the postfrontal clouds. To compare with

392 observations, the model data are processed by: (a) selecting the grids at a distance from the

393 simulated cell center similar to the distance of the airplane position from the observed postfrontal

394 cell center, and sampling the data at a similar ambient temperature as observed by the aircraft

395 (around -10 ºC along the horizontal segment shown in Fig. 6a); (b) accounting for the location

396 mismatch and increasing the sample size in the simulation to be more representative by

397 extending the sampling area to include 20 grids at the front and back of a selected grid along the

398 flight track, mimicking approximately the distance traveled by the G-1 airplane in five minutes;

399 (c) filtering out the sampled grids with values of (LWC + IWC) below the detection limit of

400 WCM (i.e., 0.02 g m^{-3}, Thompson et al., 2016). Both horizontal and vertical flight segments are

401 incorporated for comparison.

402   Figure 6c and d shows comparisons of LWC, IWC, and the glaciation ratio of

403 IWC/(IWC+LWC) between the simulations and aircraft measurements. The LWC is

404 overestimated in all three simulations with DM15+MC18 of the largest overestimation (6 times

405 higher than observations), while IWC is underestimated in Bigg and DM15 (nearly an order of

406 magnitude lower in DM15 than observations) (Fig. 6c). DM15+MC18 predicts much higher

407 IWC than the other two simulations, with an overestimation of IWP by ~3 times. The mean

408 glaciation ratios fall in the range of 0.1- 0.9 among the simulations (Fig. 6d), indicating that the

409 observed mixed-phase cloud feature is simulated by the model. DM15+MC18 shows a mean

410 ratio of ~ 0.70, similar to the observed value of 0.74. This shows that the mixed-phase state is

411 well captured when the marine INP effect is considered. In contrast, in Bigg and DM15 with a

412 glaciation ratio of 0.41 or less, the mixed-phase state is liquid-dominated. The inclusion of the

413 marine INP effect improves the simulation of cloud phase states via enhancing heterogeneous ice

414 formation through immersion freezing. These results also show that post-frontal clouds are very

415 sensitive to marine INPs. A detailed examination of how the marine INPs impact ice nucleation

416 and cloud properties will be discussed in the following section.

417

418 **4.2 Marine INP effects under different AR stages**

419   Impacts of the marine INPs transported from the Pacific Ocean on orographic clouds and

420 precipitation are revealed by comparing the simulation of DM15+MC18 with the simulation of

421 DM15.

422   As described in Section 3 about the AR evolution, before AR landfall (from 06:00 UTC 5

423 to 18:00 UTC 6 February), precipitation occurred in northern California. After AR landfall (from

424 18:00 UTC 6 to 12:00 UTC 7 February), heavy orographic precipitation along the Sierra Nevada

425 Mountains occurred (Fig. 7a). At the post-AR stage (from 12:00 UTC 7 to 09:00 UTC 8

426 February), scattered postfrontal cloud cells formed, with relatively small cloud fractions and

427 precipitation (Fig. 7a). The mean water vapor and temperature profiles are very different

428 between different AR stages, but the two simulations – DM15 (blue) and DM15+MC18 (red) –

429 predict very similar results as seen from the overlapping blue and red lines.

430   From the time series of average precipitation rates (Fig. 7a), the effect of marine INPs

431   varies with the different AR stages, from the large increases of precipitation (over 50% in

432   general) before AR landfall (the red dotted line, second y-axis) to no significant effects (a very

433   small increase) after AR landfall. In the first stage (before AR landfall), the total precipitation

434   increases by 36% on average due to the marine INP effect (Fig. 7a and Table 1). There is only a

435   4% increase in the total precipitation after AR landfall. Note that precipitation is very small at

436   some point before AR landfall, so the large increases might not mean that much. The total

437   precipitation at the post-AR stage is also small and the change in domain-mean precipitation

438   from DM15 and DM15+MC18 is negligible. Thus, the marine INP effect only significantly

439   increases the total precipitation over the domain at the stage before AR landfall when a moderate

440   amount of precipitation occurs in northern California (Fig. 8a). After AR landfall, precipitation

441   increases significantly. Although the total precipitation is not changed much by the marine INPs,

442   the marine INPs produce a spillover effect featuring reduced precipitation on the windward slope

443   of the mountains but increase precipitation over the lee side (Fig. 8b and Fig. 9e). This is because

444   with the marine INPs, the larger amount of ice/snow that forms on the windward slope is

445   transported to the lee side (Fig. 9d) and grows to a larger size and precipitates as snow. This

446   spillover effect is accompanied by a large reduction of cloud water and rain over the windward

447   side because of the conversion of liquid to ice (Fig. 9b-c). Since the water vapor transport along

448   the cross-section is very similar between DM15 and DM15+MC18 (Fig. 9a), the spillover effect

449   by marine INPs is mainly the result of different cloud microphysical properties instead of

450   meteorological conditions.

451   Even though the total domain precipitation is not changed much by the marine INPs at

452   the latter two stages, the cloud phase and the near-surface precipitation type (i.e., rain or snow)

453   are notably changed (Table 1). The mean glaciation ratio in the mixed-phase is very low in

454   DM15 (0.14, 0.16, and 0.001 for the 1st, 2nd, and 3rd stages, respectively) and is increased in

455   DM15+MC18 to 0.74, 0.59, and 0.36, respectively. We examine the ratio of snow/(rain+snow)

456   in mass mixing ratio at the lowest model level for the changes of the near-surface precipitation

457   type (Fig. 7b). There is negligible snow precipitation near the surface in DM15 and the ratios of

458   snow precipitation are very small during the entire AR event. The snow precipitation ratios

459   increase in DM15+MC18 and the magnitudes vary significantly with different AR stages. On

460   average, the ratio of snow precipitation increases from 0.002, 0.001, <0.001 in DM15 to 0.08,

461   0.04, and 0.13 in DM15+MC18 before AR landfall, after AR landfall, and post-AR, respectively

462   (Table 1). This shows that marine INPs increase snow precipitation and the effect is particularly

463   significant before AR landfall and post-AR. Correspondingly, rain precipitation is reduced

464   (Table 1). This has an important implication for the regional hydrological resource since more

465   snow accumulation in winter increases freshwater resources in the summer while less rain

466   reduces flood risks.

467   The increased snow and reduced rain at the surface correspond to the increased ice water

468   path (IWP) and decreased liquid water path (LWP; Fig. 7c). The mean LWP in DM15+MC18 is

469   reduced by 66%, 46%, and 26% for the three stages relative to DM15, respectively (Table 1). We

470   showed an increased LWC from DM15 to DM15+MC18 in Fig. 6c in the postfrontal cells. Here

471   the decrease in LWC/LWP averaged over the entire post-AR stage is dominated by the strong

472   decrease over the time before the postfrontal cloud formed. Both LWC and IWC are increased by

473   marine INPs as shown in Fig. 6 (see section 4.3 for more discussion). IWP is greatly enhanced

474   by about 8, 5, and 440 times at the three stages, respectively. Interestingly, the total condensate

475   water path (TWP) is increased by the marine INPs (Fig. 7d). On average there are 45%, 29%,

476   and 35% increases in TWP in DM15+MC18 at the three AR stages relative to DM15,

477   respectively (Table 1). The increases in the total condensate water path and the increased surface

478   precipitation (or no change) suggest that marine INPs enhance the conversion of water from the

479   vapor phase to the condensate phase, which will be further discussed later. This is particularly

480   the case before AR landfall, with water vapor content notably reduced in DM15+MC18

481   compared with DM15 (Fig. S3a).

482   Cloud cover is slightly increased during the first two stages (4-5%) in the simulations

483   considering marine INPs, but the change at the post-AR stage is ~ 20% on average, which is very

484   significant. Because both TWP and cloud cover are increased due to the marine INP effect, the

485   cloud radiative forcing (CRF) at TOA gets stronger by 15%, 13%, and 10% for the three AR

486   stages, respectively. Although the cloud phase, precipitation type, and cloud fraction at the post-

487   AR stage have the largest changes among the three stages by the marine INP effect (Table 1), the

488   CRF does not change drastically probably because of the offset between the increase resulting

489   from the increased cloud fraction and TWP and the decrease from the reduced cloud liquid is the

490   largest.

491   Overall, the marine INP effects on TWP, IWP, and snow precipitation are more

492   significant at the first and third stages (i.e., before AR landfall and post-AR) than the stage after

493   AR landfall, but a notable spillover effect is seen after AR made landfall. Cloud and

494   precipitation quantities are more sensitive to marine INPs before AR landfall than after AR

495   landfall, and the responses of TWP/IWP and snow precipitation are particularly drastic at the

496   post-AR stage (Table 1). The reasons leading to the different responses at different AR stages are

497   now examined.

4.3 Explaining different marine INP effects at different AR stages

We first examine the temporal evolution of dust and marine aerosol number concentrations, which are derived based on the predicted mass mixing ratios as described in Section 2 and used as input to the DeMott et al. (2015) and MC2018 parameterizations (Fig. 10a, b), as well as their corresponding immersion freezing (i.e., ice nucleation) rates (Fig. 10c, d). The dust concentrations and the corresponding ice nucleation rates (Fig. 10a, c) are about three orders of magnitude lower than those of the marine aerosols (Fig. 10b, d) during the AR events. Ice nucleation from dust is negligible at temperatures warmer than -15 ºC but the ice nucleation from marine aerosols is notable. This is mainly because of three orders of magnitude higher marine aerosol number concentrations from the surface up to 8 km since ice nucleation efficiencies of marine aerosols are about three orders of magnitude lower than mineral dust at any temperature (MC2018). The deep marine aerosol layer during the AR allows notable ice nucleation at temperatures even higher than -15 ºC. Homogenous freezing (< -37 ºC; Fig. 10d vs. 10c) occurs less in DM15+MC18 because of a larger consumption of liquid drops and supersaturation in the heterogeneous freezing regime. This is commonly seen in convective clouds (e.g., Zhao et al. 2019). The clear-sky marine aerosol number concentrations increase from before AR landfall to post-AR as the AR evolved (Fig. 10b). After the AR made landfall, marine aerosols increase significantly as AR strong winds near the ocean surface produce more of them and also transport more to the Sierra Nevada Mountains (Fig. 10b). Despite the significant increase in marine aerosols after AR landfall, the marine INP effects on clouds and precipitation are small at this stage, because the increase of marine aerosols does not increase ice nucleation rates (Fig. 10d). However, at the post-AR stage, the ice nucleation rates from the marine INPs are up to a few

520   times larger than the earlier two stages (Fig. 10d), explaining why the effects on IWP and snow

521   precipitation at the post-AR stage are largest among the three stages.

522   To further understand how and why cloud and precipitation responses to marine INPs are

523   different at different AR stages, we separate clouds into three cloud regimes: a shallow warm

524   cloud regime with cloud top temperature (CTT) warmer than 0 $^\circ$C, a mixed-phase cloud regime

525   with CTT between -30 and 0 $^\circ$C, and a deep cloud regime having CTT colder than -30 $^\circ$C and

526   cloud base temperatures above 0 $^\circ$C. Figure 11 shows that the marine INP effect consistently

527   shifts the cloud occurrences from the shallow warm cloud regime to mixed-phase and/or deep

528   cloud regimes among the three AR stages. It is noted that the deep cloud regime is enhanced

529   much more at the first and third stages than the second stage, i.e., 22% before AR landfall and

530   235% at the post-AR stage but only 8% after AR landfall. The post-AR stage also has the largest

531   increase in mixed-phase cloud occurrences.

532   Accordingly, the mean cloud depth for each cloud regime is changed by marine INPs,

533   with a decrease for the shallow warm clouds and an increase for the mixed-phase and deep

534   clouds (Fig. 11b). Before AR landfall, the increase in the deep cloud depth is largest while at the

535   post-AR stage, the increase in the mixed-phase cloud depth is the largest. Consistent with a shift

536   in cloud regimes, the total precipitation produced by shallow warm clouds is reduced by 9%,

537   22%, and 16% while the total precipitation produced by deep clouds is increased by 66%, 4%,

538   and 350%, respectively, at the three AR stages (Fig. 11c). Therefore, the large increase in the

539   surface accumulated precipitation by marine INPs before AR landfall (36%) is mainly because of

540   the increase in deep cloud precipitation. The larger occurrence of deep clouds at this stage is

541   consistent with a larger increase in TWP and reduction in moisture. Although the relative

542   increases in deep cloud occurrences and precipitation by marine INPs are very large at the post-

543   AR stage, their occurrences are so small that their contribution to the total precipitation is

544   negligible.

545   How do marine INPs reduce shallow warm clouds but increase mixed-phase and deep

546   clouds and why is this effect larger at the first and third stages? Marine INPs greatly enhance ice

547   and snow number concentrations and mass mixing ratios through immersion freezing, which

548   converts drops to ice or snow particles (Figs. 12a and 13a). The mean number concentrations

549   and mass mixing ratios of ice particles (ice +snow) in mixed-phase and deep cloud regimes are

550   several orders of magnitude higher in DM15+MC18 than in DM15. As detailed in Fan et al.

551   (2017a) which studied the same type of mixed-phase clouds in the same region, more ice/snow

552   particles forming from the immersion freezing enhance the Wegener–Bergeron–Findeisen

553   (WBF) and riming processes (Table 2), converting supercooled drops to ice or snow and leading

554   to more ice/snow but fewer cloud droplets and raindrops (Figs. 12b, c and 13b, c). The

555   reductions of cloud droplet and raindrop number concentrations and mass mixing ratios from

556   DM15 to DM15+MC18 are larger before AR landfall and during post-AR relative to the stage

557   after AR landfall, corresponding to a larger shift to the mixed-phase and deep clouds. Thus, the

558   larger increases in deposition/WBF and riming rates are seen (Table 2).

559   As discussed earlier, the largest ice nucleation rates from marine aerosols at the post-AR

560   stage explain the largest marine INP effects among the three stages. The factors contributing to

561   the larger ice nucleation rates include the increased abundance of marine aerosols compared to

562   the previous two stages (Fig. 10b). In addition, with the ~ 6 ºC colder temperatures below 8-km

563   altitudes during the post-AR stage compared to the other two stages, ice nucleation from marine

564   aerosols becomes more efficient (Fig. 10d). The most significantly invigorated postfrontal cloud

565   cells by the marine INP effect (i.e., the increase in both LWC and IWC and a large increase in

566   cloud fraction) might also be related to small scale thermodynamic changes through the feedback

567   of microphysical changes over the first two AR stages.

568   As for why increases of deep cloud occurrence and precipitation are less significant after

569   AR landfall compared to before AR landfall, first, the moisture increase after AR landfall occurs

570   in the lower atmosphere while the middle- and upper-level atmosphere are much drier than

571   before AR landfall (Fig. 2d), which favors more warm clouds and rain but is less favorable to ice

572   cloud development as indicated by the smallest ratio of snow precipitation (Fig. 7b). For more

573   warm clouds/rain-dominated situations, the enhancement of ice formation would have less

574   influence. Furthermore, in the drier conditions aloft, more ice formation means less efficient

575   growth, thus the impacts on IWC/IWP and precipitation would be smaller. Cloud dynamics

576   (vertical velocity) is not changed much by the marine INP effect at all three stages, indicating

577   that the feedback from the increased latent heating resulting from enhanced deposition and

578   riming does not play an important role here, likely because this is not a convective environment.

579   **5 Conclusion and discussion**

580   We have explored the effects of INPs from sea spray aerosols transported from the

581   Pacific Ocean on wintertime mixed-phase stratiform cloud properties and precipitation

582   associated with atmospheric river (AR) events. This is done by carrying out simulations at a

583   cloud-resolving scale (1 km) using WRF-Chem coupled with the spectral-bin microphysics

584   (SBM) scheme for an AR event observed during the 2015 Atmospheric Radiation Measurement

585   Cloud Aerosol Precipitation Experiment (ACAPEX). We have implemented ice nucleation

586   parameterization for sea spray aerosols (McCluskey et al. 2018a) into SBM to account for the

587   marine INP effect. By comparing with available airborne and ground-based observations, we

588   show that considering the marine INP effect in the model improves the simulation of cloud phase

589   states (i.e., increased glaciation ratio) and precipitation.

590   Through enhancing ice and snow formation, marine INPs greatly enhance WBF and

591   riming processes, which convert liquid clouds to mixed-phase and ice clouds. There is a notable

592   shift in cloud occurrences with reduced shallow warm clouds (44%, 26%, and 7% for before and

593   after AR landfall and the post-AR stages, respectively) and increased mixed-phase (10%, 7%,

594   and 38%) and/or deep cloud regimes (~ 22%, 8%, and 230%) because of the marine INP effect.

595   As a result, large increases in the ice water path (5 times or more), total condensate water path

596   (29% or more), and the ratio of snow precipitation (40 times or more) are seen. There is an

597   enhanced conversion of water from the vapor phase to the condensate phase so the water vapor is

598   generally reduced with the marine INP effect considered.

599   The significance of the above-described marine INP effects varies with the AR stages,

600   with a larger effect before AR landfall and post-AR than after AR landfall that has the dominant

601   precipitation. Note that the marine INP effects on cloud properties and snow precipitation are

602   still notable even at the stage after AR landfall. Although the total precipitation is not much

603   changed, the drastic increase of snow precipitation and reduced rain precipitation at the surface

604   have an important implication for the regional water resources and flood risks since more snow

605   increases freshwater resources while less rain reduces flash flood risks. In addition, at this stage,

606   the marine INPs produce a notable spillover effect with a precipitation decrease (up to 30%) over

607   the windward slope of the mountains but precipitation (snow) over the lee side is doubled,

608   because more ice/snow formed over the windward side falls slower than rain and is more easily

609   transported to the lee side.

610   Several factors can be responsible for the smaller marine INP effects on cloud properties

611   (particularly reduction of shallow warm clouds and increased mixed-phase and deep clouds) and

612   snow precipitation after AR landfall compared with before AR landfall. First, after AR landfall,

613   the moisture is heavily concentrated at the lower atmosphere while the middle- and upper-level

614   atmosphere is much drier than before AR landfall. Therefore, the environment is more warm

615   cloud and rain dominated, limiting the effects of enhanced ice formation. Furthermore, in drier

616   conditions, more ice formation means less efficient growth, thus the impacts on IWC/IWP and

617   precipitation would be smaller.

618   The post AR stage has the largest response of the cloud regime shift and snow

619   precipitation among the three stages, because of the largest ice nucleation rates from the marine

620   aerosols. The larger ice nucleation rates compared with the other two stages are probably

621   because the abundance of marine aerosols is increased and also with ~ 6 ºC colder temperatures

622   below 8-km altitudes than the other two stages, ice nucleation from the deep marine aerosol layer

623   is more efficient.

624   This study suggests that the inclusion of marine INPs enhances orographic precipitation

625   mainly through more efficient growth (deposition and riming) of a larger number of ice particles

626   than liquid droplets, which is consistent with literature studies (Mühlbauer and Lohmann, 2009;

627   Fan et al., 2014, 2017; Xiao et al., 2015). The spillover effect by the increase of CCN has been

628   presented in several previous studies (e.g., Mühlbauer and Lohmann, 2008, 2009; Saleeby et al.,

629   2011, 2013; Carrio and Cotton, 2014; Letcher and Cotton, 2014). To our knowledge, this study is

630   the first to show the spillover effect associated with the INP effect. The prominent spillover

631   effect by the marine INP is different from Fan et al. (2014, 2017) that did not find such an effect

632   by dust INPs. There are a couple of factors that might be responsible for the difference. First,

633   marine INPs are mainly brought by ARs so the windward side gets INP first while dust INPs are

634   not associated with AR so there is no temporal sequence to have dust between the windward and

635   Lee sides. Second, the AR event is different with a different wind direction and speed, which

636   makes the transport of ice/snow to the lee side easier in this case.

637   The marine INP effect revealed in this study is clearly manifested due to the very low

638   dust INP concentrations for this particular situation and the high abundance of marine aerosols

639   during the AR which allows notable ice nucleation even at temperatures higher than -15 ºC. This

640   higher abundance of marine aerosols overcomes the fundamental lower efficiency of marine

641   INPs compared to dust INPs. With high dust INPs, the effects of marine INPs might not be as

642   significant since they compete for supercooled liquid drops. Although this is a single case study,

643   the AR event and its evolution are representative. Thus, the study suggests the importance of

644   accounting for marine aerosols as INPs, in addition to long-range transported mineral dust, to

645   simulate winter clouds and precipitation in the western United States in regional and global

646   climate models. We employ an empirical parameterization for marine INPs developed from the

647   data collected over the northern Atlantic Ocean and use sea salt aerosols as a surrogate of sea

648   spray aerosols, which might produce some uncertainties. Nevertheless, the marine INP

649   parameterization appears representative of this region based on Levin et al. (2019). More

650   observational data are needed in the western U.S. for (a) developing ice nucleation

651   parameterizations for potentially variable marine organics and (b) understanding marine organics

652   emission and chemical mechanisms and accurately simulating marine organics in the model. As

653   discussed earlier, the conversion of mass to number concentrations over each aerosol bin might

654   introduce some uncertainty to this study, which calls for model developments of predicting the

655   number concentration of each aerosol component.

656

Data availability.

The observational data can be accessed from the ARM data archive,

https://www.arm.gov/research/campaigns/amf2015apex. The model simulation data will be

available through the NERSC data repository after the paper is accepted.

661

Supplement.

The supplement related to this article is available online at:

664

Author contributions.

JF designed the study and model experiments. YL, JF, and PL performed numerical simulations

and analyses. JF and YL wrote the paper and other authors commented on it. LRL, PJD, LG, JF,

JT, YL, and JHJ contributed by either processing data including model input and observational

data or participating in the discussion of results.

670

Competing interests.

The authors declare that they have no conflict of interest.

Acknowledgments.

This research used resources of the PNNL Institutional Computing (PIC), and National Energy

Research Scientific Computing Center (NERSC). NERSC is a U.S. DOE Office of Science User

Facility operated under Contract No. DE-AC02-05CH11231. Funding for ACAPEX that

provides data collected on the G-1 aircraft was supported by the Atmospheric Radiation

Measurement (ARM) user facility, a U.S. Department of Energy (DOE) Office of Science user

679   facility managed by the Office of Biological and Environmental Research. The deployment of

680   the G-1 also involved the assistance of many PNNL/ARM field staff including M. Hubbell and

681   C. Eveland who flew the G-1 during ACAPEX. The authors acknowledge California Air

682   Resources Board for providing the 2015 emission inventory data and Dr. Allen White from

683   NOAA's Physical Sciences Laboratory for providing rainfall gauge data, and thank Alyssa

684   Matthews and Jingyu Wang at PNNL and Yuan Wang at JPL for technical/data discussion.

685

686   **Financial support.**

687   This study was supported by the Office of Science of U.S. Department of Energy Biological and

688   Environmental Research through the Regional and Global Model Analysis program area that

689   supports the Water Cycle and Climate Extremes Modeling (WACCEM) Science Focus Area at

690   PNNL and the DOE Early Career Research Program (project # 70071). PNNL is operated for the

691   U.S. Department of Energy (DOE) by Battelle Memorial Institute under contract DE-AC05-

692   76RL01830.

693 **Reference**

694 Ault, A. P., Williams, C. R., White, A. B., Neiman, P. J., Creamean, J. M., Gaston, C. J., Ralph,
695   F. M., and Prather, K. A.: Detection of Asian dust in California orographic precipitation, J.
696   Geophys. Res.-Atmo., 116, 1–15, https://doi.org/10.1029/2010JD015351, 2011.
697 Baumgardner, D., Brenguier, J. L., Bucholtz, A., Coe, H., DeMott, P., Garrett, T. J., Gayet, J. F.,
698   Hermann, M., Heymsfield, A., Korolev, A., Kramer, M., Petzold, A., Strapp, W., Pilewskie,
699   P., Taylor, J., Twohy, C., Wendisch, M., Bachalo, W., and Chuang, P.:Airborne instruments
700   to measure atmospheric aerosol particles, clouds and radiation: A cook's tour of mature and
701   emerging technology, Atmos. Res., 102(1), 10–29, 10.1016/j.atmosres.2011.06.021, 2011.
702 Bigg, E. K.: The Formation of Atmospheric Ice Crystals by the Freezing of Droplets, Q. J. Roy.
703   Meteorol. Soc., 79, 510–519, https://doi.org/10.1002/qj.49707934207, 1953.
704 Burrows, S. M., Hoose, C., Pöschl, U., and Lawrence, M. G.: Ice nuclei in marine air: Biogenic
705   particles or dust?, Atmos. Chem. Phys., 13, 245–267, https://doi.org/10.5194/acp-13-245-
706   2013, 2013.
707 Carrió, G.G., Cotton, W.R., 2014. On the buffering of CCN impacts on wintertime orographic
708   clouds: an idealized examination, Atmos. Res. 137, 136–144.
709 Chen, F. and Dudhia, J.: Coupling an Advanced Land Surface–Hydrology Model with the Penn
710   State–NCAR MM5 Modeling System. Part I: Model Implementation and Sensitivity, Mon.
711   Weather Rev., 129, 569–585, https://doi.org/https://doi.org/10.1175/1520-
712   0493(2001)129<0569:Caalsh>2.0.Co;2, 2001.
713 Choularton, T. W. and Perry, S. J.: A model of the orographic enhancement of snowfall by the
714   seeder-feeder mechanism, Q. J. Roy. Meteorol. Soc., 112, 335–345,
715   https://doi.org/https://doi.org/10.1002/qj.49711247204, 1986.
716 Choudhury, G., B. Tyagi, J. Singh, C. Sarangi, S.N. Tripathi. Aerosol-orography-precipitation –
717   a critical assessment, Atmos. Environ., 214 (116831) (2019), pp. 1-19,
718   10.1016/j.atmosenv.2019.116831.
719 Cordeira, J. M., Ralph, F. M., Martin, A., Gaggini, N., Spackman, J. R., Neiman, P. J., Rutz, J. J.,
720   and Pierce, R.: Forecasting atmospheric rivers during CalWater 2015, Bull Am. Meteorol.
721   Soc., 98, 449–459, https://doi.org/10.1175/BAMS-D-15-00245.1, 2017.
722 Creamean, J. M., Suski, K. J., Rosenfeld, D., Cazorla, A., DeMott, P. J., Sullivan, R. C., White,
723   A. B., Ralph, F. M., Minnis, P., Comstock, J. M., Tomlinson, J. M., and Prather, K. A.: Dust
724   and Biological Aerosols from the Sahara and Asia Influence Precipitation in the Western
725   U.S, Science, 339, 1572–1578, https://doi.org/10.1126/science.1227279, 2013.
726 Creamean, J. M., Ault, A. P., White, A. B., Neiman, P. J., Ralph, F. M., Minnis, P., and Prather,
727   K. A.: Impact of interannual variations in sources of insoluble aerosol species on orographic
728   precipitation over California's central Sierra Nevada, Atmos. Chem. Phys., 15, 6535–6548,
729   https://doi.org/10.5194/acp-15-6535-2015, 2015.
730 DeMott, P. J., Prenni, A. J., Liu, X., Kreidenweis, S. M., Petters, M. D., Twohy, C. H.,
731   Richardson, M. S., Eidhammer, T., and Rogers, D. C.: Predicting global atmospheric ice
732   nuclei distributions and their impacts on climate, Proc. Nat. Acad. Sci. U.S.A., 107, 11217–
733   11222, https://doi.org/10.1073/pnas.0910818107, 2010.
734 DeMott, P. J., Prenni, A. J., McMeeking, G. R., Sullivan, R. C., Petters, M. D., Tobo, Y.,
735   Niemand, M., Möhler, O., Snider, J. R., Wang, Z., and Kreidenweis, S. M.: Integrating
736   laboratory and field data to quantify the immersion freezing ice nucleation activity of

737   mineral dust particles, Atmos. Chem. Phys., 15, 393–409, https://doi.org/10.5194/acp-15-
738   393-2015, 2015.
739 DeMott, P. J., Hill, T. C. J., McCluskey, C. S., Prather, K. A., Collins, D. B., Sullivan, R. C.,
740   Ruppel, M. J., Mason, R. H., Irish, V. E., Lee, T., Hwang, C. Y., Rhee, T. S., Snider, J. R.,
741   McMeeking, G. R., Dhaniyala, S., Lewis, E. R., Wentzell, J. J. B., Abbatt, J., Lee, C.,
742   Sultana, C. M., Ault, A. P., Axson, J. L., Martinez, M. D., Venero, I., Santos-Figueroa, G.,
743   Stokes, M. D., Deane, G. B., Mayol-Bracero, O. L., Grassian, V. H., Bertram, T. H.,
744   Bertram, A. K., Moffett, B. F., and Franc, G. D.: Sea spray aerosol as a unique source of ice
745   nucleating particles, Proc. Nat. Acad. Sci. U.S.A., 113, 5797–5803,
746   https://doi.org/10.1073/pnas.1514034112, 2016.
747 Dettinger, M. D., Ralph, F. M., Das, T., Neiman, P. J., and Cayan, D. R.: Atmospheric Rivers,
748   Floods and the Water Resources of California, Water-Sup., 3(2), 445-478,
749   https://doi.org/10.3390/w3020445, 2011.
750 Fan, J., Leung, L. R., Li, Z., Morrison, H., Chen, H., Zhou, Y., Qian, Y., and Wang, Y.: Aerosol
751   impacts on clouds and precipitation in eastern China: Results from bin and bulk
752   microphysics, J. Geophys. Res., 117, https://doi.org/https://doi.org/10.1029/2011jd016537,
753   2012.
754 Fan, J., Leung, L. R., DeMott, P. J., Comstock, J. M., Singh, B., Rosenfeld, D., Tomlinson, J.
755   M., White, A., Prather, K. A., Minnis, P., Ayers, J. K., and Min, Q.: Aerosol impacts on
756   California winter clouds and precipitation during CalWater 2011: local pollution versus
757   long-range transported dust, Atmos. Chem. Phys., 14, 81–101, https://doi.org/10.5194/acp-
758   14-81-2014, 2014.
759 Fan, J., Han, B., Varble, A., Morrison, H., North, K., Kollias, P., Chen, B., Dong, X.,
760   Giangrande, S. E., Khain, A., Lin, Y., Mansell, E., Milbrandt, J. A., Stenz, R., Thompson,
761   G., and Wang, Y.: Cloud-resolving model intercomparison of an MC3E squall line case:
762   Part I—Convective updrafts, J. Geophys. Res.-Atmo., 122, 9351–9378,
763   https://doi.org/10.1002/2017JD026622, 2017a.
764 Fan, J., Leung, L. R., Rosenfeld, D., and DeMott, P. J.: Effects of cloud condensation nuclei and
765   ice nucleating particles on precipitation processes and supercooled liquid in mixed-phase
766   orographic clouds, Atmos. Chem. Phys., 17, 1017–1035, https://doi.org/10.5194/acp-17-
767   1017-2017, 2017b.
768 Fast, J. D., Gustafson Jr., W. I., Easter, R. C., Zaveri, R. A., Barnard, J. C., Chapman, E. G.,
769   Grell, G. A., and Peckham, S. E.: Evolution of ozone, particulates, and aerosol direct
770   radiative forcing in the vicinity of Houston using a fully coupled meteorology-chemistry-
771   aerosol model, J. Geophys. Res.-Atmo., 111,
772   https://doi.org/https://doi.org/10.1029/2005jd006721, 2006.
773 French, J. R., Friedrich, K., Tessendorf, S. A., Rauber, R. M., Geerts, B., Rasmussen, R. M.,
774   Xue, L., Kunkel, M. L., and Blestrud, D. R.: Precipitation formation from orographic cloud
775   seeding, Proc. Nat. Acad. Sci. U.S.A., 115, 1168 LP – 1173,
776   https://doi.org/10.1073/pnas.1716995115, 2018.
777 Gao, W., Fan, J., Easter, R. C., Yang, Q., Zhao, C., and Ghan, S. J.: Coupling spectral-bin cloud
778   microphysics with the MOSAIC aerosol model in WRF-Chem: Methodology and results for
779   marine stratocumulus clouds, J. Adv. Model. Earth Syst., 8, 1289–1309,
780   https://doi.org/10.1002/2016MS000676.Received, 2016.

Geerts, B., Miao, Q., Yang, Y., Rasmussen, R., and Breed, D.: An Airborne Profiling Radar Study of the Impact of Glaciogenic Cloud Seeding on Snowfall from Winter Orographic Clouds, J. Atmos. Sci., 67, 3286–3302, https://doi.org/10.1175/2010JAS3496.1, 2010.

Glienke, S. and Mei, F.: Two-Dimensional Stereo (2D-S) Probe Instrument Handbook. Ed. by Robert Stafford, ARM user facility. DOE/SC-ARM-TR-233. 10.2172/1597436, 2019.

Glienke, S. and Mei, F.: Fast Cloud Droplet Probe (FCDP) Instrument Handbook. Ed. by Robert Stafford, ARM user facility. DOE/SC-ARM-TR-238. 10.2172/1597469, 2020.

Goldberger, L. A.: Passive Cavity Aerosol Spectrometer Probe Aboard Aircraft (PCASP-AIR) with Signal Processing Package 200 Instrument Handbook. Ed. by Robert Stafford, ARM user facility. DOE/SC-ARM-TR-241, 2020.

Gong, S. L., Barrie, L. A., and Blanchet, J. P.: Modeling sea-salt aerosols in the atmosphere 1. Model development, J. Geophys. Res.-Atmo., 102, 3805–3818, https://doi.org/10.1029/96jd02953, 1997a.

Gong, S. L., Barrie, L. A., Prospero, J. M., Savoie, D. L., Ayers, G. P., Blanchet, J. P., and Spacek, L.: Modeling sea-salt aerosols in the atmosphere 2. Atmospheric concentrations and fluxes, J. Geophys. Res.-Atmo., 102, 3819–3830, https://doi.org/10.1029/96jd03401, 1997b.

Gourley, J., B. Kaney, and Maddox R.: Evaluating the calibrations of radars: A software approach. Preprints, 31st Int. Conf. on Radar Meteorology, Seattle, WA, Amer. Meteor. Soc., 459–462, 2003.

Gourley, J. J., Illingworth, A. J., and Tabary, P: Absolute Calibration of Radar Reflectivity Using Redundancy of the Polarization Observations and Implied Constraints on Drop Shapes, J. Atmos. Ocean Technol., 26(4), 689-703, 2009

Guenther, A. B., Jiang, X., Heald, C. L., Sakulyanontvittaya, T., Duhl, T., Emmons, L. K., and Wang, X.: The Model of Emissions of Gases and Aerosols from Nature version 2.1 (MEGAN2.1): an extended and updated framework for modeling biogenic emissions, Geosci. Model Dev., 5, 1471–1492, https://doi.org/https://doi.org/10.5194/gmd-5-1471-2012, 2012.

Hazra, A., Padmakumari, B., Maheskumar, R. S., and Chen, J. P.: The effect of mineral dust and soot aerosols on ice microphysics near the foothills of the Himalayas: A numerical investigation, Atmos. Res., 171, 41–55, https://doi.org/10.1016/j.atmosres.2015.12.005, 2016.

Helmus, J. J. and Collis, S. M.: The Python ARM Radar Toolkit (Py-ART), a library for working with weather radar data in the Python programming language, J. Open Res. Software, 4, e25, https://doi.org/10.5334/jors.119, 2016

Hoose, C., Kristjánsson, J. E., and Burrows, S. M.: How important is biological ice nucleation in clouds on a global scale?, Environ. Res. Lett., 5, 24009, https://doi.org/10.1088/1748-9326/5/2/024009, 2010.

Iacono, M. J., Delamere, J. S., Mlawer, E. J., Shephard, M. W., Clough, S. A., and Collins, W. D.: Radiative forcing by long-lived greenhouse gases: Calculations with the AER radiative transfer models, J. Geophys. Res.-Atmo., 113, https://doi.org/https://doi.org/10.1029/2008jd009944, 2008.

Janjić, Z. I. and Prediction, N. C. for E.: Nonsingular implementation of the Mellor-Yamada level 2.5 scheme in the NCEP Meso model, 2001.

Kanji, Z. A., Ladino, L. A., Wex, H., Boose, Y., Burkert-Kohn, M., Cziczo, D. J., and Krämer, M.: Overview of Ice Nucleating Particles, Meteorol. Monogr. 58, 1.1-1.33, https://doi.org/10.1175/amsmonographs-d-16-0006.1, 2017.

827 Khain, A., Lynn, B., and Dudhia, J.: Aerosol Effects on Intensity of Landfalling Hurricanes as
828   Seen from Simulations with the WRF Model with Spectral Bin Microphysics, J. Atmos.
829   Sci., 67, 365–384, https://doi.org/doi:10.1175/2009JAS3210.1, 2010.
830 Khain, A. P., Leung, L. R., Lynn, B., and Ghan, S.: Effects of aerosols on the dynamics and
831   microphysics of squall lines simulated by spectral bin and bulk parameterization schemes, J.
832   Geophys. Res.-Atmo., 114, https://doi.org/10.1029/2009jd011902, 2009.
833 Korolev, A. v, Isaac, G. A., Cober, S. G., Strapp, J. W., and Hallett, J.: Microphysical
834   characterization of mixed-phase clouds, Q. J. Roy. Meteorol. Soc., 129, 39–65,
835   https://doi.org/https://doi.org/10.1256/qj.01.204, 2003.
836 Letcher, T., Cotton, W.R., 2014. The effect of pollution aerosol on wintertime orographic
837   precipitation in the Colorado Rockies using a simplified emissions scheme to predict CCN
838   concentrations, J. Appl. Meteorol. Climatol. 53 (4), 859–872.
839 Levin, E. J. T., DeMott, P. J., Suski, K. J., Boose, Y., Hill, T. C. J., McCluskey, C. S., Schill, G.
840   P., Rocci, K., Al-Mashat, H., Kristensen, L. J., Cornwell, G., Prather, K., Tomlinson, J.,
841   Mei, F., Hubbe, J., Pekour, M., Sullivan, R., Leung, L. R., and Kreidenweis, S. M.:
842   Characteristics of Ice Nucleating Particles in and Around California Winter Storms, J.
843   Geophys. Res.-Atmo., 124, 11530–11551, https://doi.org/10.1029/2019JD030831, 2019.
844 Lin, Y., Fan, J., Jeong, J.-H., Zhang, Y., Homeyer, C. R., and Wang, J.: Urbanization-Induced
845   Land and Aerosol Impacts on Storm Propagation and Hail Characteristics, J. Atmos. Sci.,
846   78, 925–947, https://doi.org/10.1175/jas-d-20-0106.1, 2020.
847 Martin, A. C., Cornwell, G., Beall, C. M., Cannon, F., Reilly, S., Schaap, B., Lucero, D.,
848   Creamean, J., Martin Ralph, F., Mix, H. T., and Prather, K.: Contrasting local and long-
849   range-transported warm ice-nucleating particles during an atmospheric river in coastal
850   California, USA, Atmos. Chem. Phys., 19, 4193–4210, https://doi.org/10.5194/acp-19-
851   4193-2019, 2019.
852 Matthews, A., F. Mei, and Comstock, J.: Water content monitor (WCM-2000), ARM Airborne
853   Facility (AAF). Atmospheric Radiation Measurement (ARM) Climate Research Facility
854   Data Archive, data set acquired 27 Jan 2015 and accessed 10 Jan 2016, 2015.
855 McCluskey, C. S., Ovadnevaite, J., Rinaldi, M., Atkinson, J., Belosi, F., Ceburnis, D., Marullo,
856   S., Hill, T. C. J., Lohmann, U., Kanji, Z. A., O'Dowd, C., Kreidenweis, S. M., and DeMott,
857   P. J.: Marine and Terrestrial Organic Ice-Nucleating Particles in Pristine Marine to
858   Continentally Influenced Northeast Atlantic Air Masses, J. Geophys. Res.-Atmo., 123,
859   6196–6212, https://doi.org/10.1029/2017JD028033, 2018a.
860 McCluskey, C. S., Hill, T. C. J., Humphries, R. S., Rauker, A. M., Moreau, S., Strutton, P. G.,
861   Chambers, S. D., Williams, A. G., McRobert, I., Ward, J., Keywood, M. D., Harnwell, J.,
862   Ponsonby, W., Loh, Z. M., Krummel, P. B., Protat, A., Kreidenweis, S. M., and DeMott, P.
863   J.: Observations of Ice Nucleating Particles Over Southern Ocean Waters, Geophys. Res.
864   Lett., 45, 11,989-11,997, https://doi.org/10.1029/2018GL079981, 2018b.
865 Mellor, G. L. and Yamada, T.: Development of a turbulence closure model for geophysical fluid
866   problems, Rev. Geophys., 20, 851–875,
867   https://doi.org/https://doi.org/10.1029/RG020i004p00851, 1982.
868 Meyers, M. P., DeMott, P. J., and Cotton, W. R.: New Primary Ice-Nucleation Parameterizations
869   in an Explicit Cloud Model, J. Appl. Meteorol., 31, 708–721, https://doi.org/10.1175/1520-
870   0450(1992)031<0708:NPINPI>2.0.CO;2, 1992.

871 Muhlbauer, A., Lohmann, U.: Sensitivity studies of the role of aerosols in warm- phase
872   orographic precipitation in different dynamical flow regimes. J. Atmos. Sci. 65 (8), 2522–
873   2542, 2008.
874 Muhlbauer, A. and Lohmann, U.: Sensitivity studies of aerosol-cloud interactions in mixed-
875   phase orographic precipitation, J. Atmos. Sci., 66, 2517–2538,
876   https://doi.org/10.1175/2009JAS3001.1, 2009.
877 Murray, B. J., O'Sullivan, D., Atkinson, J. D., and Webb, M. E.: Ice nucleation by particles
878   immersed in supercooled cloud droplets, Chem. Soc. Rev., 41, 6519–6554,
879   https://doi.org/10.1039/c2cs35200a, 2012.
880 Niemand, M., Möhler, O., Vogel, B., Vogel, H., Hoose, C., Connolly, P., Klein, H., Bingemer,
881   H., DeMott, P., Skrotzki, J., and Leisner, T.: A Particle-Surface-Area-Based
882   Parameterization of Immersion Freezing on Desert Dust Particles, J. Atmos. Sci., 69, 3077–
883   3092, https://doi.org/10.1175/jas-d-11-0249.1, 2012.
884 Ralph, F. M., Prather, K. A., Cayan, D., Spackman, J. R., DeMott, P., Dettinger, M., Fairall, C.,
885   Leung, R., Rosenfeld, D., Rutledge, S., Waliser, D., White, A. B., Cordeira, J., Martin, A.,
886   Helly, J., and Intrieri, J.: CalWater Field Studies Designed to Quantify the Roles of
887   Atmospheric Rivers and Aerosols in Modulating U.S. West Coast Precipitation in a
888   Changing Climate, Bull. Am. Meteorol. Soc., 97, 1209–1228, https://doi.org/10.1175/bams-
889   d-14-00043.1, 2016.
890 Reynolds, D. W.: A Report on Winter Snowpack-Augmentation, Bull. Am. Meteorol. Soc., 69,
891   1290–1300, https://doi.org/10.1175/1520-0477(1988)069<1290:AROWSA>2.0.CO;2, 1988.
892 Rosenfeld, D., Chemke, R., Demott, P., Sullivan, R. C., Rasmussen, R., McDonough, F.,
893   Comstock, J., Schmid, B., Tomlinson, J., Jonsson, H., Suski, K., Cazorla, A., and Prather,
894   K.: The common occurrence of highly supercooled drizzle and rain near the coastal regions
895   of the western United States, J. Geophys. Res.-Atmo., 118, 9819–9833,
896   https://doi.org/10.1002/jgrd.50529, 2013.
897 Saleeby, S.M., Cotton, W.R., Fuller, J.D.: The cumulative impact of cloud droplet nucleating
898   aerosols on orographic snowfall in Colorado, J. Appl. Meteorol. Climatol. 50 (3), 604–625,
899   2011.
900 Saleeby, S.M., Cotton, W.R., Lowenthal, D., Messina, J.: Aerosol impacts on the microphysical
901   growth processes of orographic snowfall. J. Appl. Meteorol. Climatol. 52 (4), 834–852,
902   2013.
903 Schmid, B., Tomlinson, J. M., Hubbe, J. M., Comstock, J. M., Mei, F., Chand, D., Pekour, M. S.,
904   Kluzek, C. D., Andrews, E., Biraud, S. C., and McFarquhar, G. M.: The DOE arm aerial
905   facility, Bull. Am. Meteorol. Soc., 95, 723–742, https://doi.org/10.1175/BAMS-D-13-
906   00040.1, 2014.
907 Shaw, W. J., Jerry Allwine, K., Fritz, B. G., Rutz, F. C., Rishel, J. P., and Chapman, E. G.: An
908   evaluation of the wind erosion module in DUSTRAN, Atmos. Environ., 42, 1907–1921,
909   https://doi.org/10.1016/j.atmosenv.2007.11.022, 2008.
910 Simmel, M. and Wurzler, S.: Condensation and activation in sectional cloud microphysical
911   models, Atmos. Res., 80, 218-236, 10.1016/j.atmosres.2005.08.002, 2006.
912 Thompson, D. R., McCubbin, I., Gao, B. C., Green, R. O., Matthews, A. A., Mei, F., Meyer, K.
913   G., Platnick, S., Schmid, B., Tomlinson, J., and Wilcox, E.: Measuring cloud
914   thermodynamic phase with shortwave infrared imaging spectroscopy, J. Geophys. Res.-
915   Atmo., 121, 9174–9190, https://doi.org/10.1002/2016JD024999, 2016.

Uin, J.: Ultra-High-Sensitivity Aerosol Spectrometer (UHSAS) Instrument Handbook. Ed. by
    Robert Stafford, DOE ARM Climate Research Facility. DOE/SC-ARM-TR-163, 2016.

Uno, I., Eguchi, K., Yumimoto, K., Takemura, T., Shimizu, A., Uematsu, M., Liu, Z., Wang, Z.,
    Hara, Y., and Sugimoto, N.: Asian dust transported one full circuit around the globe, Nat.
    Geosci., 2, 557–560, https://doi.org/10.1038/ngeo583, 2009.

Vali, G., DeMott, P. J., Möhler, O., and Whale, T. F.: Technical Note: A proposal for ice
    nucleation terminology, Atmos. Chem. Phys., 15, 10263–10270,
    https://doi.org/10.5194/acp-15-10263-2015, 2015.

Vergara-Temprado, J., Murray, B. J., Wilson, T. W., O'Sullivan, D., Browse, J., Pringle, K. J.,
    Ardon-Dryer, K., Bertram, A. K., Burrows, S. M., Ceburnis, D., Demott, P. J., Mason, R.
    H., O'Dowd, C. D., Rinaldi, M., and Carslaw, K. S.: Contribution of feldspar and marine
    organic aerosols to global ice nucleating particle concentrations, Atmos. Chem. Phys., 17,
    3637–3658, https://doi.org/10.5194/acp-17-3637-2017, 2017.

Xiao, H., Yin, Y., Jin, L., Chen, Q., and Chen, J.: Simulation of the effects of aerosol on mixed-
    phase orographic clouds using the WRF model with a detailed bin microphysics scheme,
    Atmos. Sci. Lett., 120, 8345–8358, https://doi.org/https://doi.org/10.1002/2014JD022988,
    2015.

Xue, L., Fan, J., Lebo, Z. et al.: Idealized Simulations of a Squall Line from the MC3E Field
    Campaign Applying Three Bin Microphysics Schemes: Dynamic and Thermodynamic
    Structure, Mon. Wea. Rev., 145, 4789- 4812, https://doi.org/10.1175/MWR-D-16-0385.1,
    2017.

Yang, Y., Sun, J., Zhu, Y., and Zhang, T.: Examination of the impacts of ice nuclei aerosol
    particles on microphysics, precipitation and electrification in a 1.5D aerosol-cloud bin
    model, J. Aerosol Sci., 140, 105440, https://doi.org/10.1016/j.jaerosci.2019.105440, 2020.

Yun, Y. and Penner, J. E.: An evaluation of the potential radiative forcing and climatic impact of
    marine organic aerosols as heterogeneous ice nuclei, Geophys. Res. Lett., 40, 4121–4126,
    https://doi.org/10.1002/grl.50794, 2013.

Zaveri, R. A., Easter, R. C., Fast, J. D., and Peters, L. K.: Model for Simulating Aerosol
    Interactions and Chemistry (MOSAIC), J. Geophys. Res.-Atmo., 113,
    https://doi.org/https://doi.org/10.1029/2007jd008782, 2008.

Zhang, Y., Fan, J., Li, Z., and Rosenfeld, D.: Impacts of Cloud Microphysics Parameterizations
    on Simulated Aerosol–Cloud-Interactions for Deep Convective Clouds over Houston,
    Atmos. Chem. Phys., 1–46, https://doi.org/10.5194/acp-2020-372, 2020.

Zhao, B., Wang, Y., Gu,Y., Liou, K.-N., Jiang, J. H., Fan, J., Liu, X., Huang, L., and Yung, Y.
    L.: Ice nucleation by aerosols from anthropogenic pollution, Nature Geosciences, 12,
    https://doi.org/10.1038/s41561-019-0389-4, 2019.

Zhao, C., Chen, S., Leung, L. R., Qian, Y., Kok, J. F., Zaveri, R. A., and Huang, J.: Uncertainty
    in modeling dust mass balance and radiative forcing from size parameterization, Atmos.
    Chem. Phys., 13, 10733–10753, https://doi.org/10.5194/acp-13-10733-2013, 2013

957   **Figures**
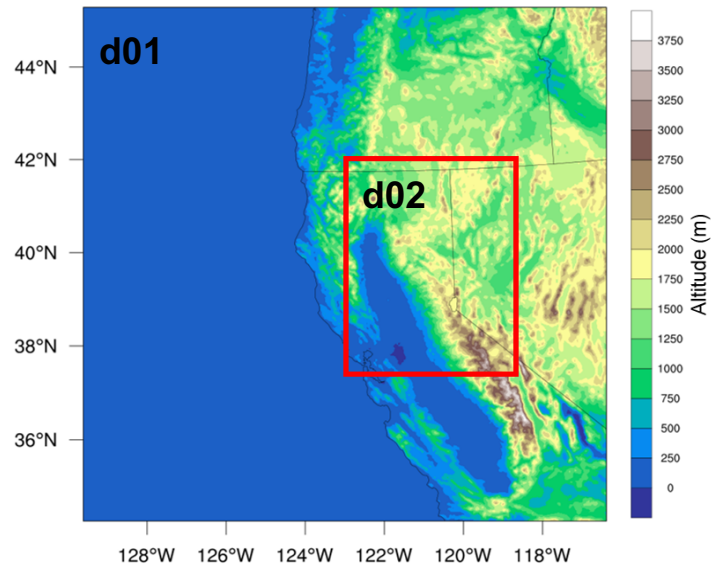
958

959   **Figure 1.** Two nested simulation domains: d01 and d02 centering over California. The color

960   shading denotes the terrain elevation.

961

962
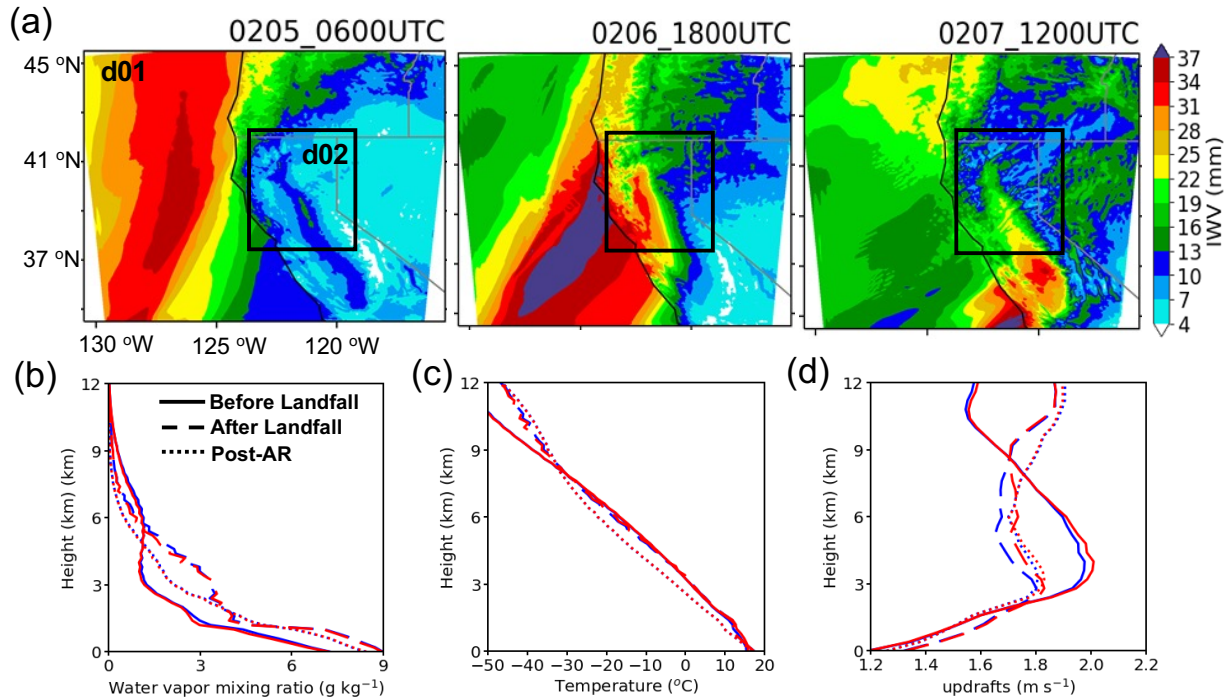
Figure 2. (a) Evolution of integrated water vapor (IWV) at 06:00 UTC 5 February (before AR landfall), 18:00 UTC 6 February (after AR landfall), and 12:00 UTC 7 February (post-AR). The black box (i.e., d02) in (a) is the domain of this study with the 5 lateral boundary grids excluded for analysis at each side. (b-d) show the mean vertical profiles of (b) water vapor mixing ratio, (c) temperature, and (d) updraft velocity at the three AR stages, i.e., before (solid lines) and after (dashed lines) AR landfall and post-AR stages (dotted lines), for the simulations of DM15 (blue) and DM15+MC18 (red). The water vapor mixing ratio and temperature are averaged for cloud-free grids, and updraft velocity is averaged over the grids with a vertical velocity greater than 1 m s⁻¹.

972
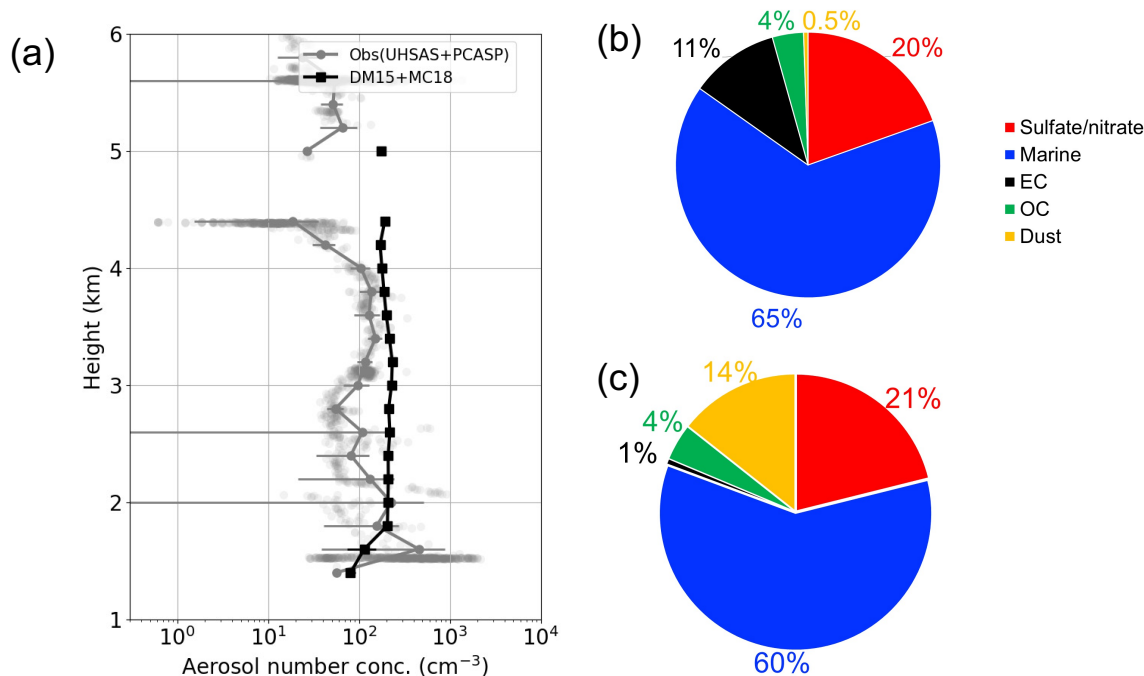
Figure 3. (a) Vertical distributions of aerosol number concentrations from aircraft observations (Obs, grey) and DM15+MC18 (black) for particles with a dry diameter over a range of 0.067~3 μm, (b) mean fractional number contributions of aerosol classifications based on measurements of single-particle mass spectra of aerosols and cloud particle residuals reported in Levin et al. (2019), and (c) mean fractional mass contributions of aerosols in DM15+MC18 (number concentration for each aerosol component is not predicted by WRF-Chem). The aerosol number concentration from aircraft observations in (a) consists of both measurements from UHSAS and PCASP. The modeled data in (a) and (c) are sampled along the aircraft route on 7 February 2015.
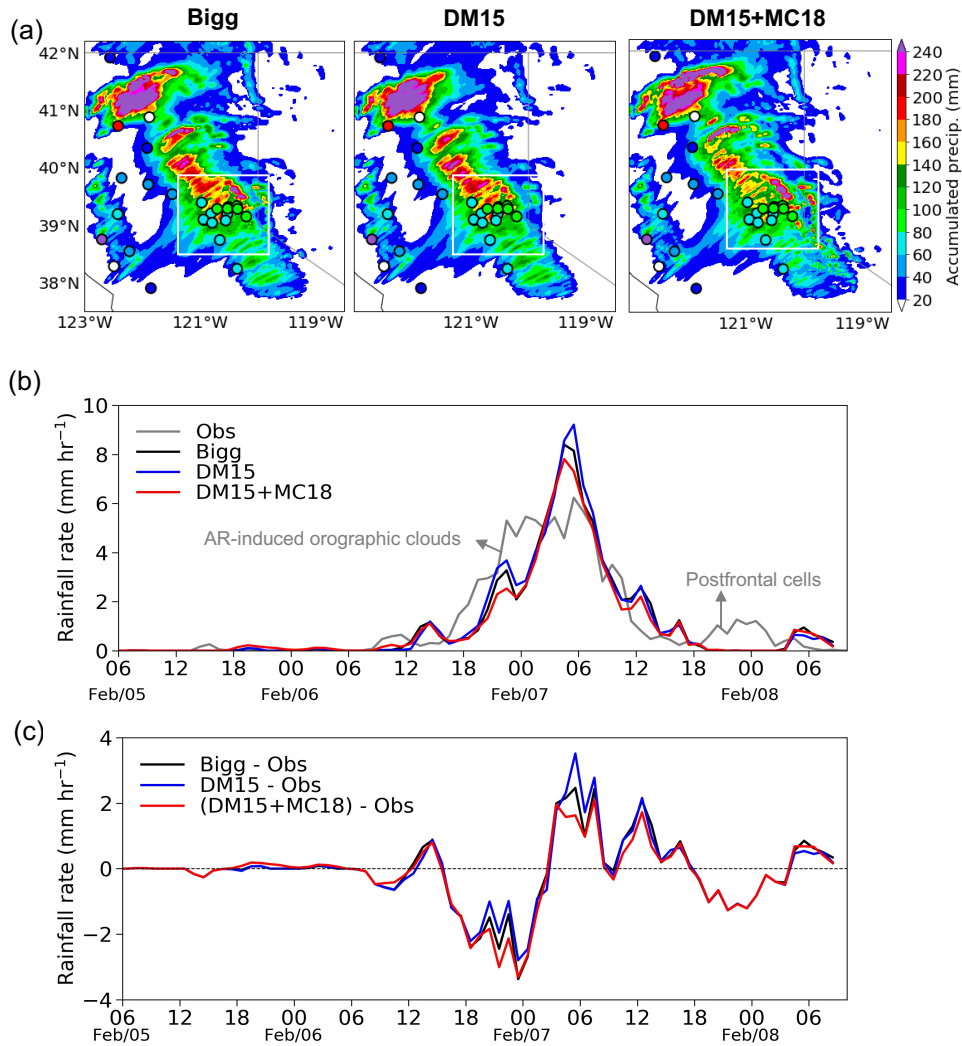
Figure 4. (a) Spatial distributions of accumulated precipitation during the AR event (5 Feb. 06:00 – 8 Feb. 09:00 UTC) from Bigg, DM15, and DM15+MC18. The color shading is for simulations and the circles denote the rain gauge measurements provided by NOAA Physical Sciences Laboratory. (b) Time series of precipitation rates during the entire AR event for rain gauge observations (grey line), Bigg (black line), DM15 (blue line), and DM15+MC18 (red line). (c) Differences between the simulations and observations based on the data of (b). The precipitation rates in (b) are averaged over all the rain gauge sites shown in (a). The white boxes in (a) mark the region where the precipitation simulation is improved by adding marine INPs.

993
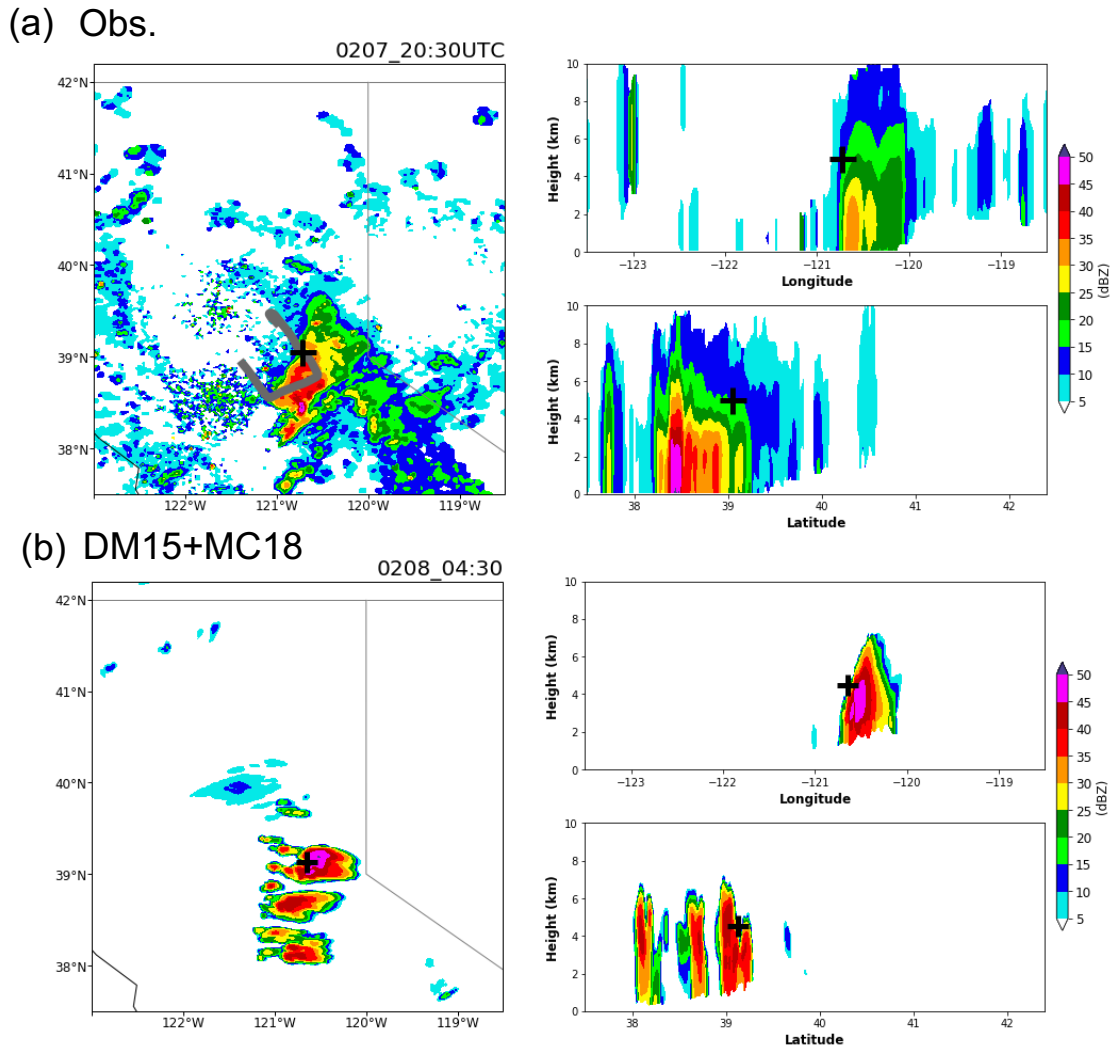
Figure 5. (a) Composite reflectivity of NEXRAD for the postfrontal clouds that the G-1 aircraft
sampled, (b) composite reflectivity from the simulation of DM15+MC18 for the postfrontal
clouds. The observation and simulation are compared at the peak reflectivity time which is 20:30
UTC 7 February for the observed clouds and 04:30 UTC 8 February for the simulated clouds.
The black crosses in the left two panels denote the positions where the longitude-height and
latitude-height cross-sections in the right panels are plotted. The grey line in the left panel of (a)
shows the flight track of the G-1 aircraft.
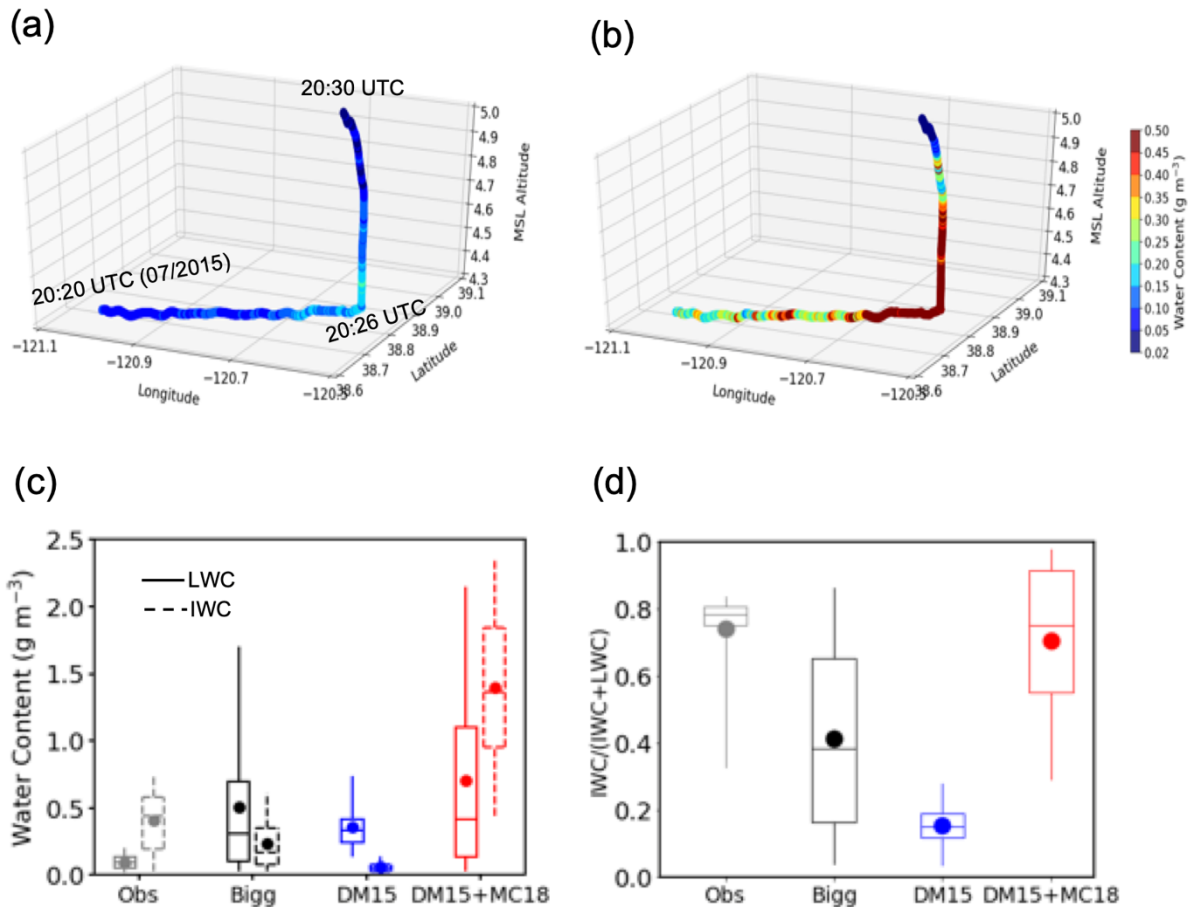
Figure 6. Comparisons of the simulations with aircraft observations. The observed (a) LWC and (b) IWC along the flight track during 20:20 – 20:30 on 7 February when the aircraft flew through the mixed-phase regime of the postfrontal clouds. (c) LWC (solid) and IWC (dashed) and (d) the glaciation ratios of IWC/(IWC+LWC) from the aircraft measurements (Obs, grey) and simulations of Bigg (black), DM15 (blue), and DM15+MC18 (red). The boxes show the 25th, median (horizontal lines in the box), and 75th percentiles of the data. The upper and lower whiskers show the 95th and 5th percentiles, respectively. The mean values are denoted by circles.
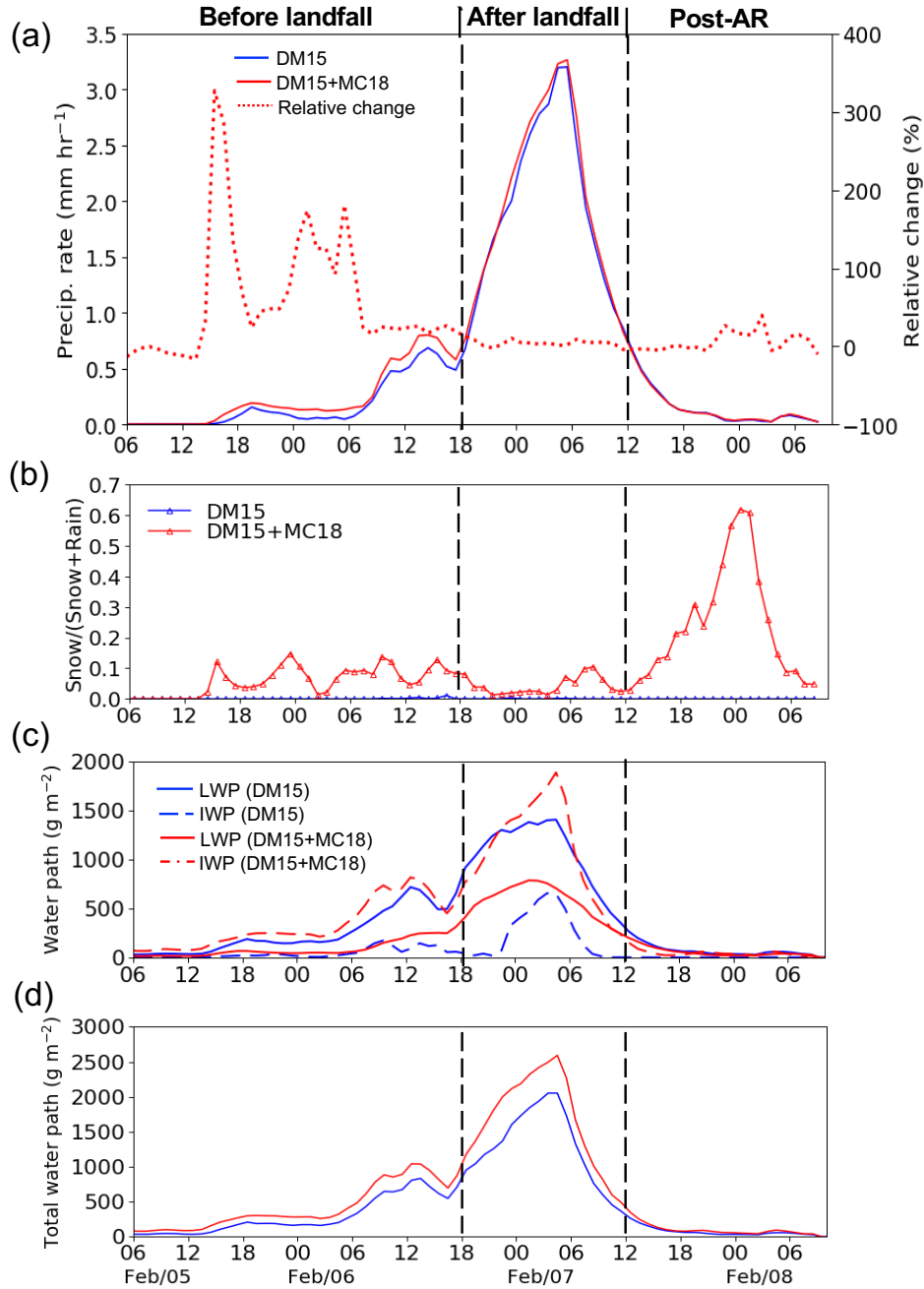
1011

1012   **Figure 7.** Time series of (a) precipitation rate (solid lines, left y-axis), (b) ratio of snow

1013   precipitation (i.e., snow/(snow+rain) in mass mixing ratio) at the lowest model level, (c) LWP

1014   (solid) and IWP (dashed) for DM15 (blue) and DM15+MC18 (red), and (d) total condensate

1015   water path (TWP). The relative changes in precipitation rate from DM15 to DM15+MC18 are

1016   shown in the red dotted line in (a) with values shown on the right y-axis. The vertical dashed

1017   lines divide the three AR stages.

1018
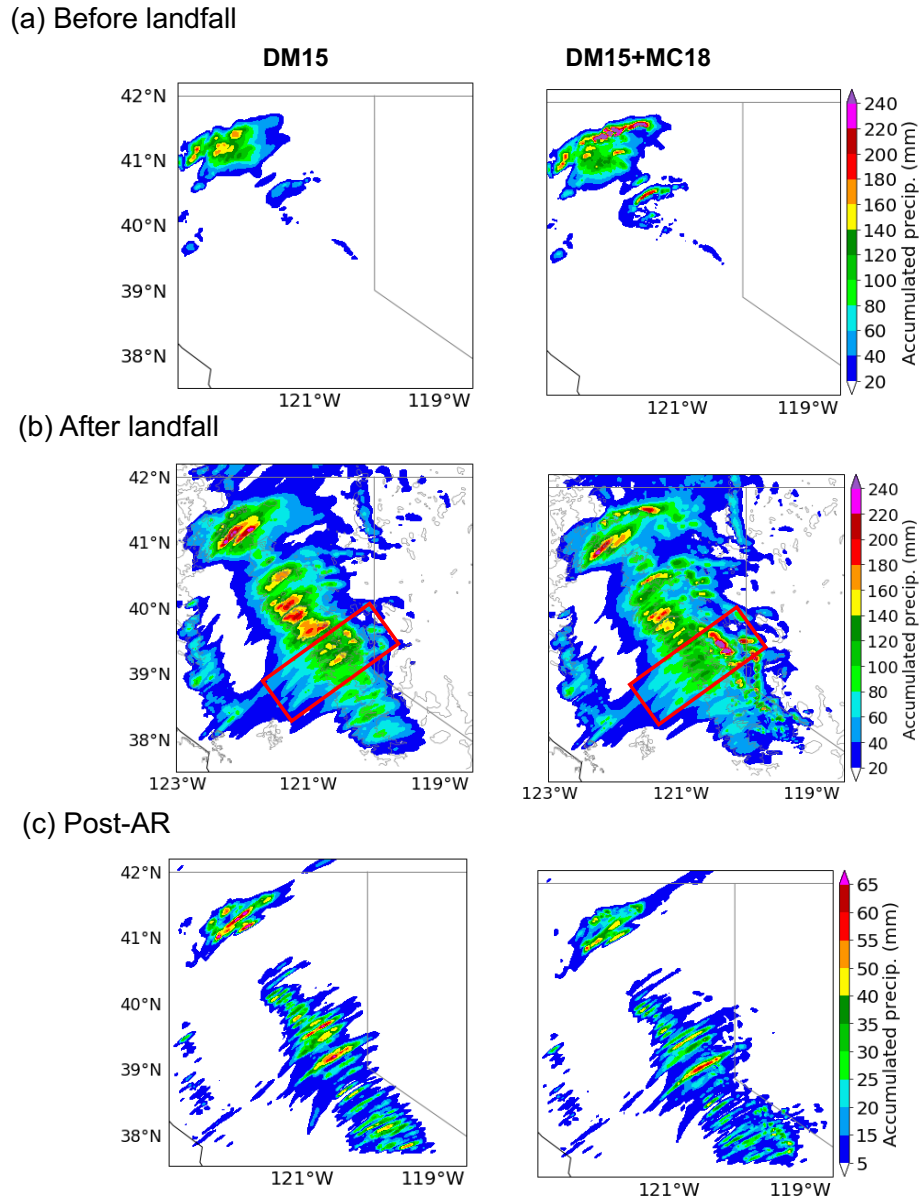
1019

1020   **Figure 8.** Spatial distribution of accumulated precipitation during the stages of (a) before AR

1021   landfall, (b) after AR landfall, and (c) post-AR in DM15 (left) and DM15+MC18 (right). The

1022   parallelograms marked in (b) denotes the area for the east-west cross-section analysis shown in

1023   Figure 9.

1024

1025

1026
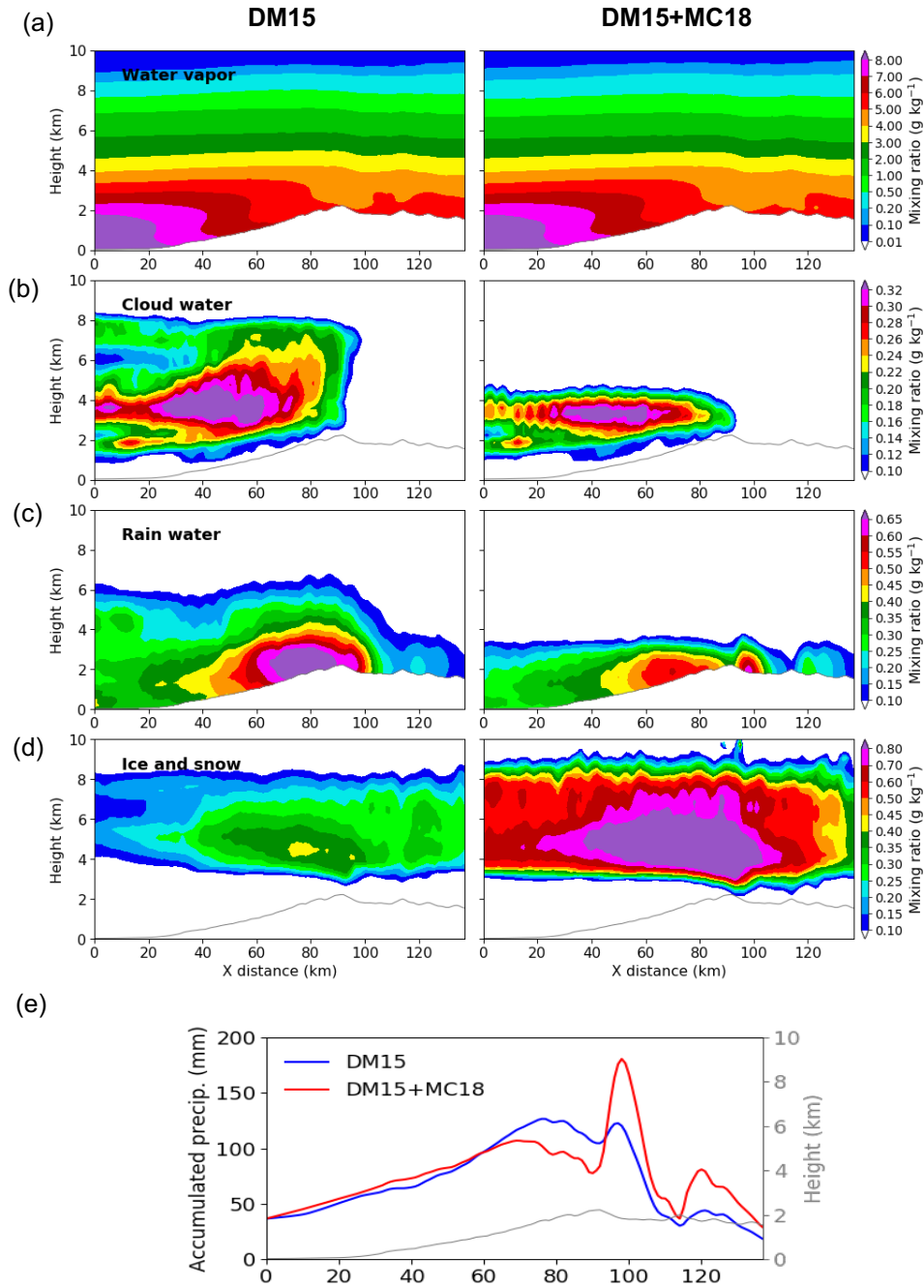
1027

1028

1029 **Figure 9.** Mean mixing ratios of (a) water vapor, (b) cloud water, (c) rainwater, (d) ice + snow,

1030 and (e) surface precipitation at the stage after AR landfall in DM15 and DM15+MC18. The

1031 vertical cross-sections are averaged over the red boxes marked in Fig. 8b and the entire stage.

1032
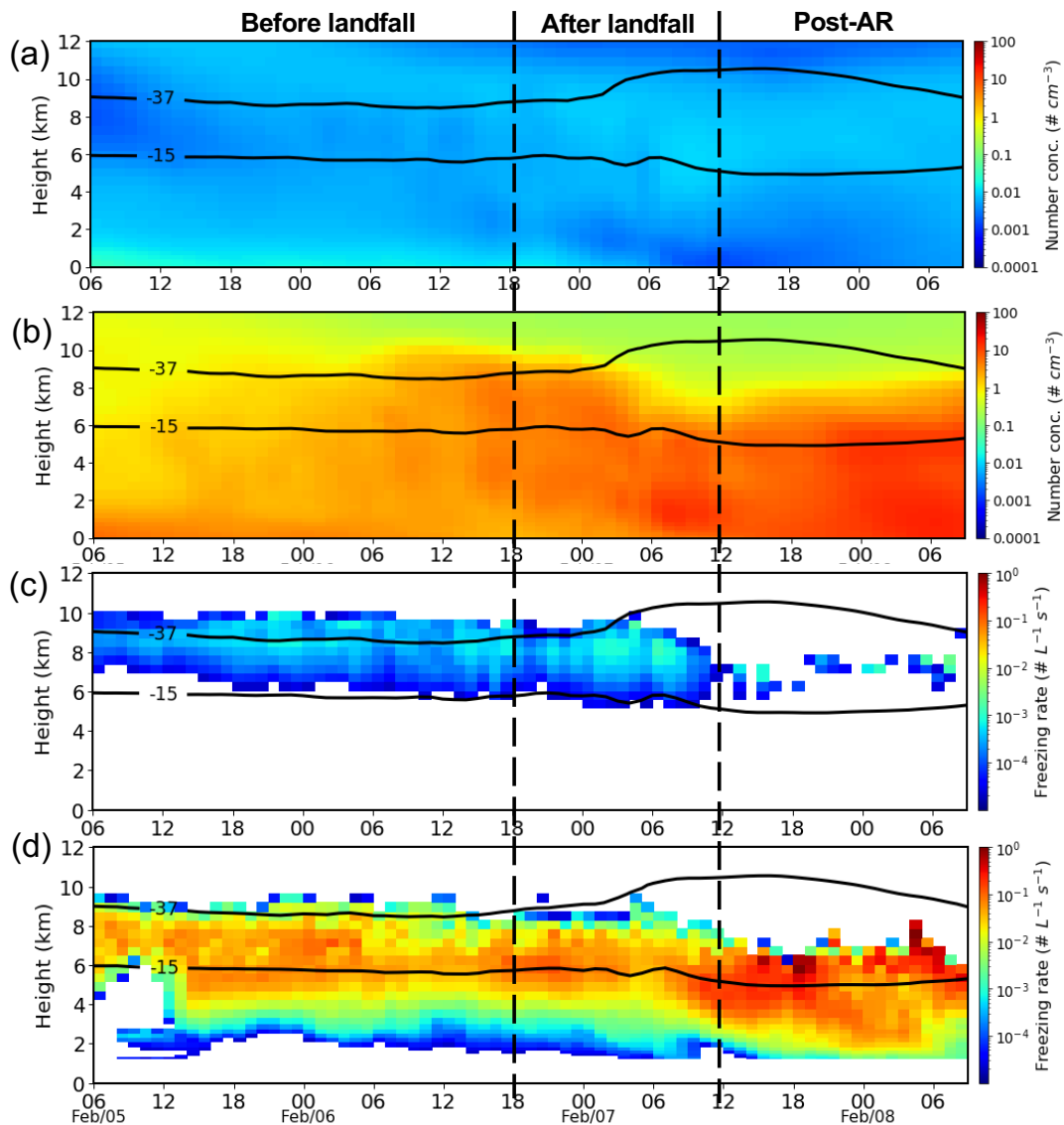
1033

1034 **Figure 10.** Time-height cross-sections of (a) dust particle (>0.5 μm) number concentration, (b)

1035 marine aerosol number concentration, (c) the freezing rate in DM15, and (d) the freezing rate in

1036 DM15+MC18. The number concentrations in (a) and (b) are derived from their corresponding

1037 mass mixing ratios under the clear-sky condition only. The freezing rates in (c) and (d) are the

1038 ice nucleation rates via immersion freezing at T > - 37 °C and the drop homogenous freezing

1039 rates at T < - 37 °C, and the values are for cloudy-points only. The black contour lines in each

1040 panel mark the temperature levels of -15 and -37 °C, representing the efficient immersion

1041 freezing temperature in DM15+MC18 and the homogeneous freezing temperature in the model,

1042 respectively.

1043
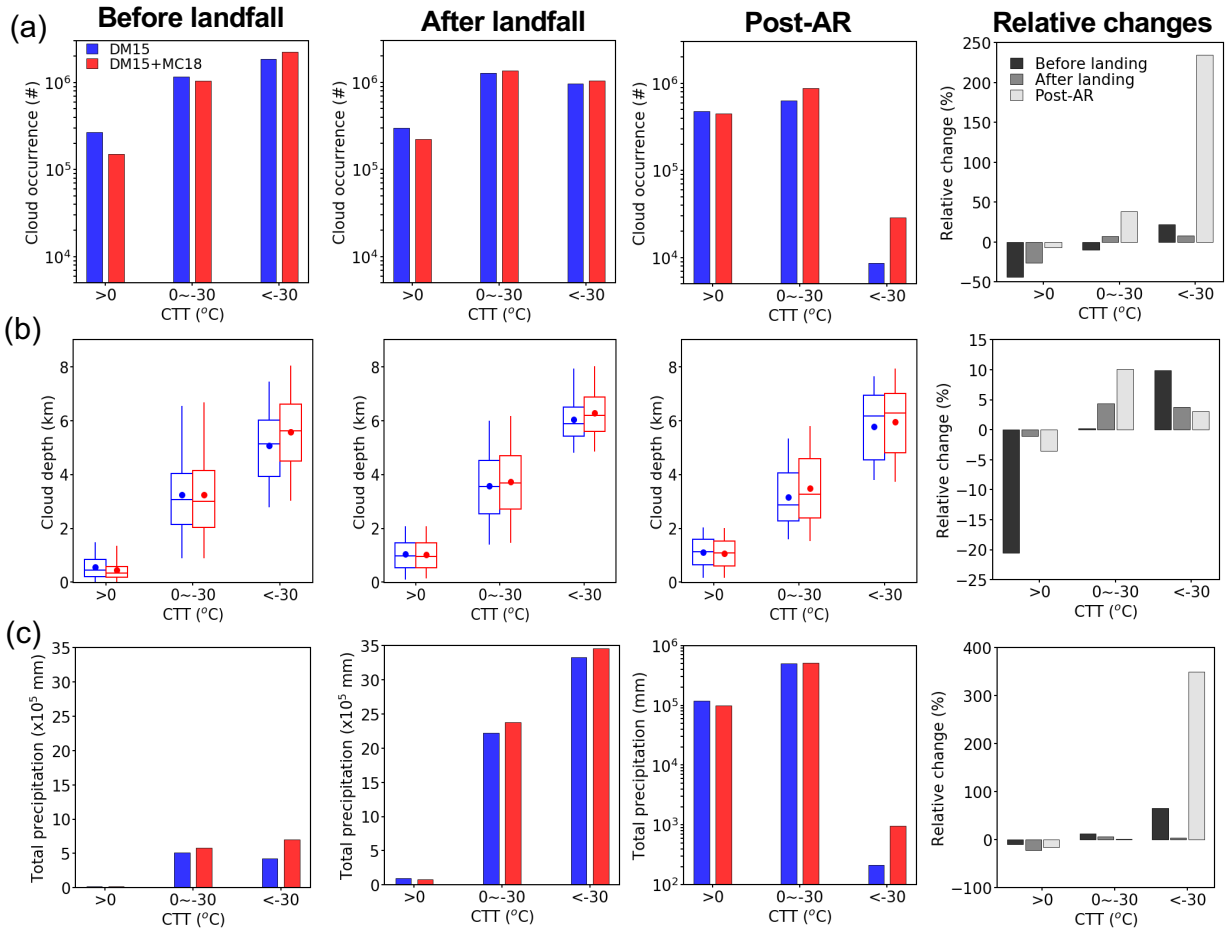
1044

1045 **Figure 11.** (a) Cloud occurrences, (b) cloud depth, and (c) total precipitation for three cloud

1046 regimes in DM15 (blue) and DM15+MC18 (red) at three AR stages from left to right: before AR

1047 landfall, after AR landfall, post-AR. The last column shows the relative changes caused by the

1048 marine INP effect, which are calculated as [(DM15+MC18) – DM15]/DM15*100%. Note that

1049 the total precipitation at the post-AR stage uses a log scale for the y-axis. The box-whisker plots

1050 follow the description in Figure 5c.
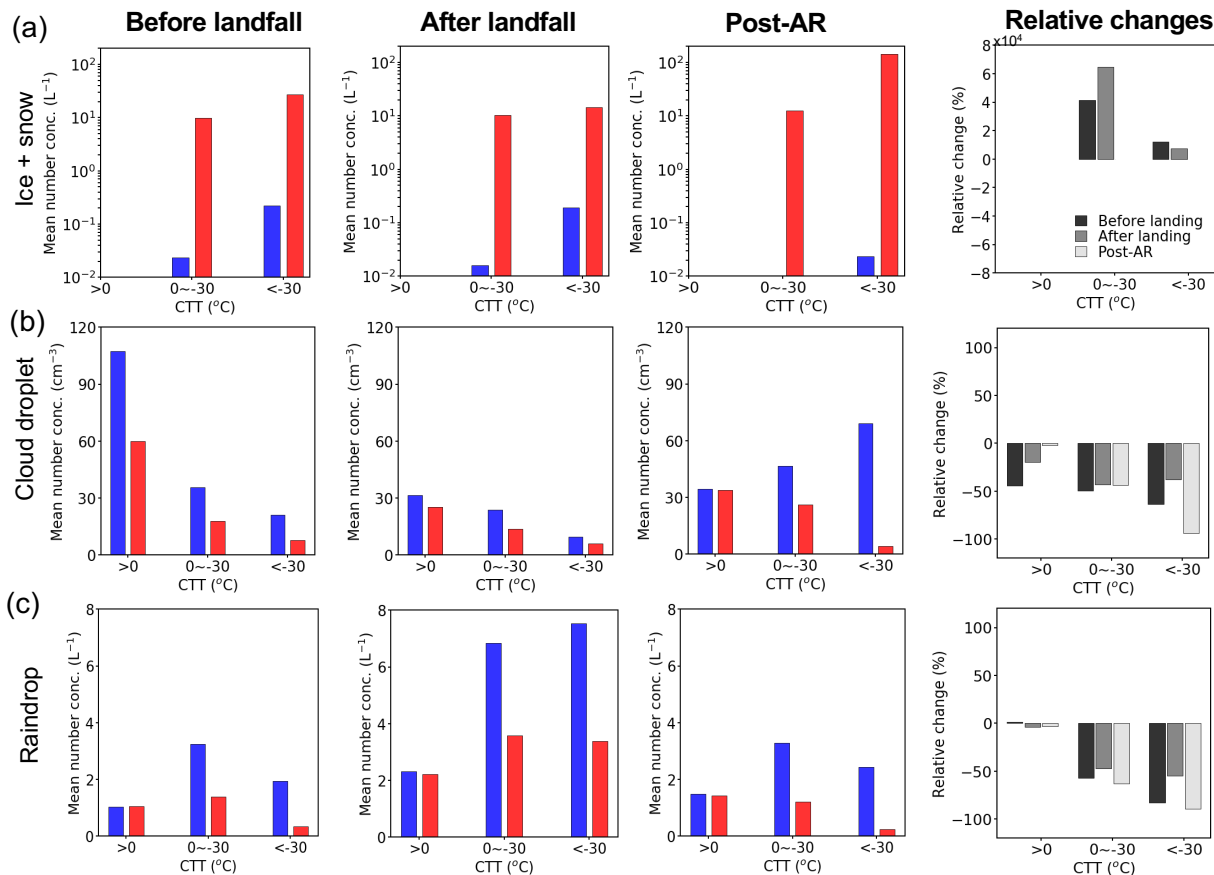
1051

1052 **Figure 12.** Hydrometeor number concentrations and their relative changes in three cloud regimes

1053 in DM15 (blue) and DM15+MC18 (red) at the three AR stages for (a) ice particles (sum of ice

1054 and snow), (b) cloud droplets, and (c) raindrops. The last column shows the relative changes

1055 caused by the marine INP effect, which are calculated as [(DM15+MC18) –

1056 DM15]/DM15*100%. Since ice particles are very limited at the post-AR stage in DM15, the

1057 percentage changes of ice particles from DM15 to DM15+MC18 are huge numbers that are

1058 omitted from the plots.
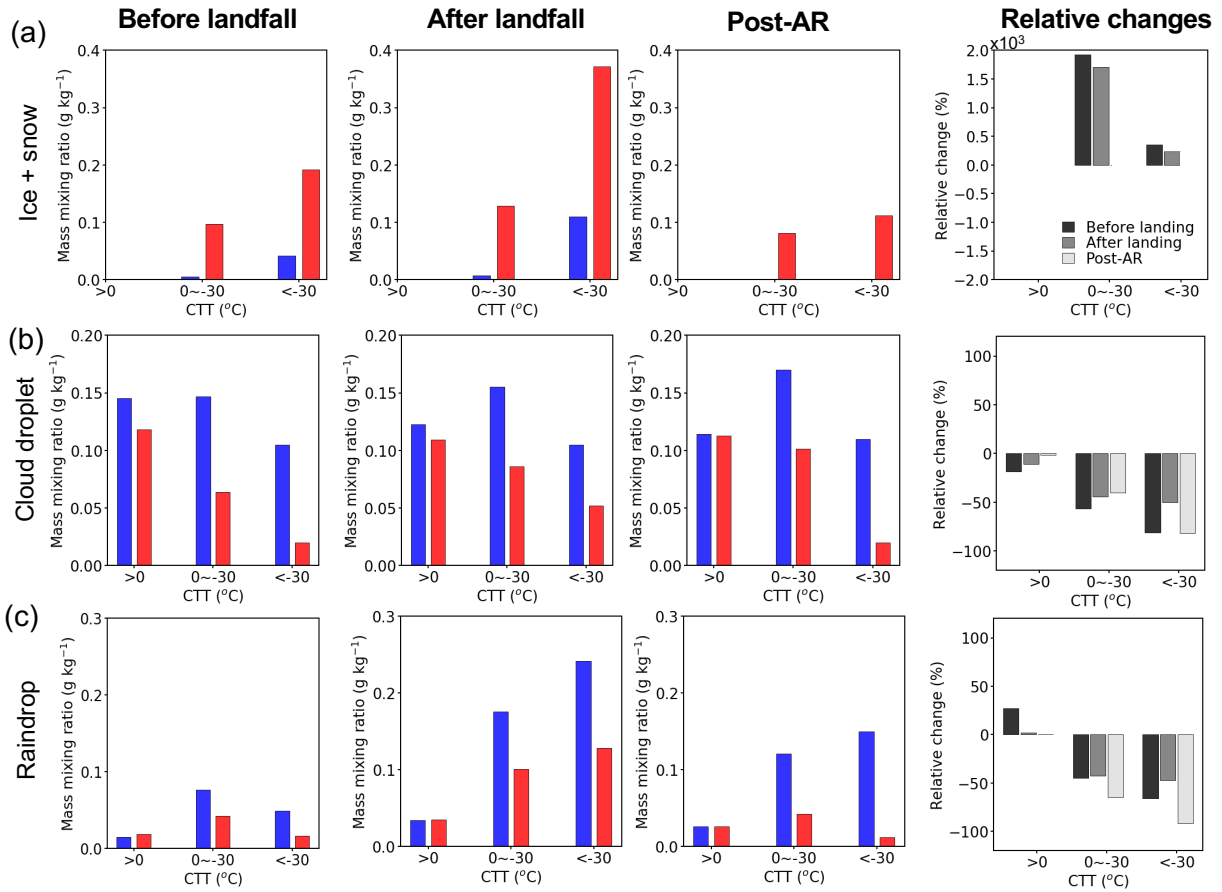
1059

1060 **Figure 13.** Same as Figure 12, except for the mass mixing ratios of (a) ice particles (sum of ice

1061 and snow), (b) cloud droplets, and (c) raindrops.

1062

1063

1064

1065

1066

1067

1068

1069

1070

1071

1072   **Table 1.** The changes in total precipitation, total condensate water path (TWP), liquid water path

1073   (LWP), and ice water path (IWP), and cloud fractions (CF), net cloud radiative forcing (CRF) at

1074   TOA from DM15 to DM15+MC18 (i.e., the marine INP effect), as well as the glaciation ratio,

1075   i.e., IWC/(LWC+IWC), and the ratios of snow precipitation, i.e., snow/(rain+snow) in mass

1076   mixing ratio at the lowest model level from DM15 to DM15+MC18, at the three AR stages. The

1077   percentage changes are calculated following ((DM15+MC18)- DM15)/DM15*100.

1078

AR stages		Before landfall	After landfall	Post-AR
Total precipitation		36%	4%	-1%
TWP		45%	29%	35%
LWP		-66%	-46%	-26%
IWP		8 times	5 times	440 times
CF		5%	4%	20%
Net CRF at TOA		15%	13%	10%
IWC/(LWC+IWC)	DM15	0.14	0.16	0.001
	DM15+MC18	0.74	0.59	0.36
Snow/(Rain+Snow)	DM15	0.002	0.001	<0.001
	DM15+MC18	0.085	0.042	0.131

1079

1080

1081 **Table 2.** The domain-mean mass rates of deposition and riming in the mixed-phase and deep

1082 cloud regimes in DM15 and DM15+MC18 at the three AR stages.

AR stages		Before landfall		After landfall		Post-AR	
		Mixed-phase clouds	Deep clouds	Mixed-phase clouds	Deep clouds	Mixed-phase clouds	Deep clouds
Deposition $(mg\ kg^{-1}\ h^{-1})$	DM15	44	171	81	388	7	8
	DM15+MC18	846	780	1128	1397	781	1013
Riming $(mg\ kg^{-1}\ h^{-1})$	DM15	27	89	57	297	25	34
	DM15+MC18	377	228	575	858	505	361

1083

1084